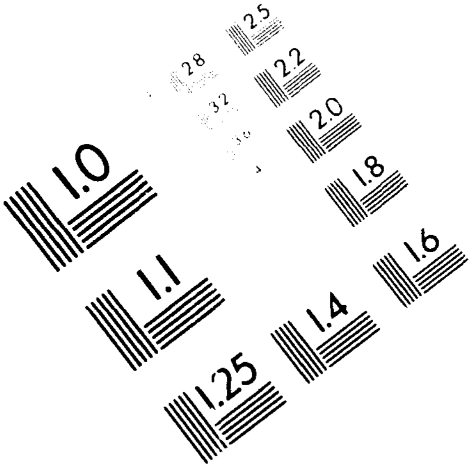

AIIM

Association for Information and Image Management

1100 Wayne Avenue, Suite 1100
Silver Spring, Maryland 20910
301/587-8202

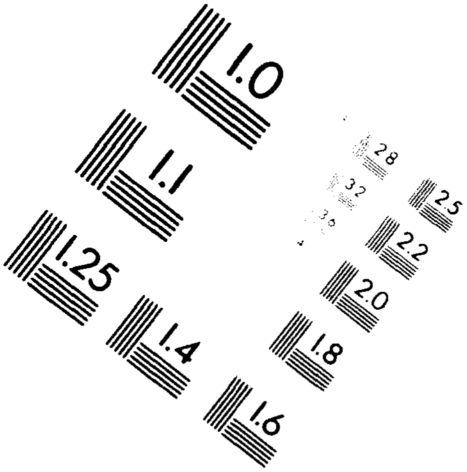

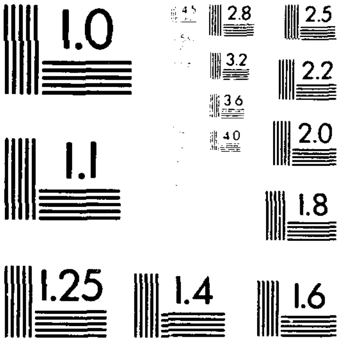

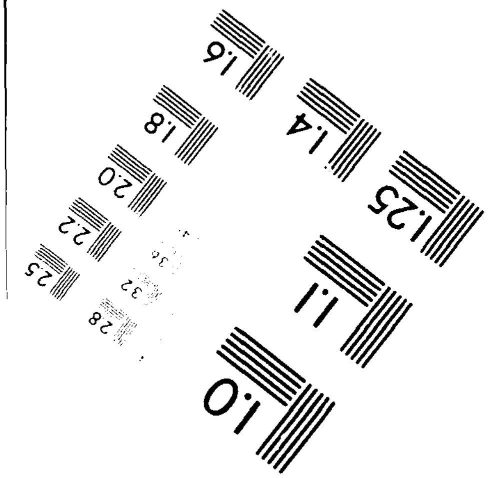

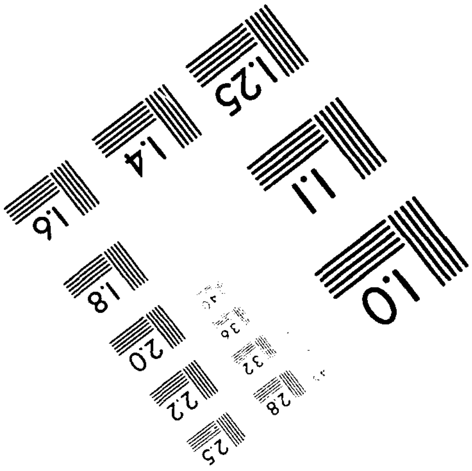

MANUFACTURED TO AIIM STANDARDS
BY APPLIED IMAGE, INC.

AD-A272 914

②

MDC 93B0465 COPY NO. ______

STRENGTH AND TOUGHNESS IMPROVEMENT OF SILICIDE INTERMETALLICS BY NANOPHASE AND MICROPHASE REINFORCEMENTS

D. S. Schwartz, R. J. Lederich, and D. A. Deuser
McDonnell Douglas Aerospace-East
St. Louis, MO 63166

S. M. L. Sastry and R. Suryanarayanan
Washington University
St. Louis, MO 63121

DTIC
ELECTE
NOV 1 9 1993
S D

October 1993
Final Technical Report for the Period 1 April 1990 - 30 April 1993

Approved for public release; distribution unlimited

The views and conclusions contained in this document are those of the authors and should not be interpreted as necessarily representing the official policies or endorsements, either expressed or implied, of the Air Force Office of Scientific Research of the U.S. Government

DTIC QUALITY INSPECTED 5

Accesion For
NTIS CRA&I ✓
DTIC TAB
Unannounced
Justification
By
Distribution /
Availability Codes
Dist | Avail and/or Special
A-1

Prepared for
UNITED STATES AIR FORCE
Air Force Office of Scientific Research
Bolling Air Force Base, DC 20332

MCDONNELL DOUGLAS AEROSPACE-EAST

93-28089

93 11 19 033

MDC 93B0465

REPORT DOCUMENTATION PAGE

Form Approved
OMB No 0704-0188

Public reporting burden for this collection of information is estimated to average 1 hour per response, including the time for reviewing instructions, searching existing data sources, gathering and maintaining the data needed, and completing and reviewing the collection of information. Send comments regarding this burden estimate or any other aspect of this collection of information, including suggestions for reducing this burden, to Washington Headquarters Services, Directorate for Information Operations and Reports, 1215 Jefferson Davis Highway, Suite 1204, Arlington, VA 22202-4302, and to the Office of Management and Budget, Paperwork Reduction Project (0704-0188), Washington, DC 20503

1. AGENCY USE ONLY *(Leave blank)*

2. REPORT DATE
8 October 1993

3. REPORT TYPE AND DATES COVERED
Final 1 April 1990-30 April 1993

4. TITLE AND SUBTITLE
Strength and Toughness Improvement of Silicide Intermetallics by Nanophase and Microphase Reinforcements

5. FUNDING NUMBERS
61102F
2306/AS

6. AUTHOR(S)
D. S. Schwartz
R. J. Lederich
D. A. Deuser
S. M. L. Sastry
R. Suryanarayanan

7. PERFORMING ORGANIZATION NAME(S) AND ADDRESS(ES)
McDonnell Douglas Aerospace-East
P.O. Box 516
St. Louis, MO 63166-0516

8. PERFORMING ORGANIZATION REPORT NUMBER
MDC 93B0465

9. SPONSORING/MONITORING AGENCY NAME(S) AND ADDRESS(ES)
USAF/AFSC
Air Force Office of Scientific Research
Building 410
Bolling Air Force Base, DC 20332-6448

10. SPONSORING/MONITORING AGENCY REPORT NUMBER
F49620-90-C-0030

11. SUPPLEMENTARY NOTES

12a. DISTRIBUTION/AVAILABILITY STATEMENT
Appr[illegible]se;
distri[illegible]

12b. DISTRIBUTION CODE
F

13. ABSTRACT *(Maximum 200 words)*

The HIP processing of $MoSi_2$ and $MoSi_2$ + Nb powder, Nb wire, and Nb foil composites was optimized. The reaction between $MoSi_2$ and Mo, W, Ta, and Nb reinforcements at 1700°C was examined. W, Ta, and Nb reinforcements formed complex, two layer reaction zones in contact with $MoSi_2$. Reaction layer growth parameters were measured for Nb. Detailed HIP modeling and deformation mechanism mapping was carried out for $MoSi_2$, $MoSi_2$ + Nb, and $MoSi_2$ + SiC. The results indicate 1400-1500°C to be optimal for producing > 98% dense material. A sensitivity analysis was developed and demonstrated for HIP modeling of TiAl and $MoSi_2$. Bend strengths of $MoSi_2$, $MoSi_2$ + Nb powder, $MoSi_2$ + 250 μm Nb wire, $MoSi_2$ + 750 μm Nb wire, and 200 μm Nb foil were measured between 20 and 1450°C in vacuum. Compositing with Nb significantly lowered elevated temperature strength. K_{Ic} was measured at 20°C for each composite and significant improvements were observed. Reinforcement morphology had a strong effect on toughness. Reinforcement morphologies listed in order of increasing potency are: Nb powder, 250 μm Nb wire, 750 μm Nb wire, Nb foil. Quantitative comparison was made between theory and measurement of the toughness increase, and poor agreement was found. HIP reaction of $MoSi_2$ and Ti powder was explored.

14. SUBJECT TERMS
Molybdenum Disilicide, Ductile Phase Toughening, Fracture Toughness, HIP Modeling, Deformation Mechanism Maps, Composites, High Temperature Intermetallics, HIP Reaction Synthesis

15. NUMBER OF PAGES
79

16. PRICE CODE

17. SECURITY CLASSIFICATION OF REPORT	18. SECURITY CLASSIFICATION OF THIS PAGE	19. SECURITY CLASSIFICATION OF ABSTRACT	20. LIMITATION OF ABSTRACT
UNCL	UNCL	UNCL	

TABLE OF CONTENTS

Section Page

LIST OF FIGURES

LIST OF FIGURES (continued)

LIST OF FIGURES (continued)

LIST OF TABLES

LIST OF PAGES

Title Page

Report Documentation Page

i-v

1 thru 74

1.0 INTRODUCTION

Critical structural components on advanced hypersonic aircraft and missiles will be exposed to temperatures above the capabilities of current structural materials. Hypersonic propulsion systems will also have service temperatures above the capabilities of the Ni-based superalloys currently employed. Materials for these applications must be strong, tough, creep and oxidation resistant, and microstructurally stable at elevated temperatures. Monolithic metallic and ceramic materials do not have the required properties, so multicomponent materials such as fiber or particulate reinforced composites must be developed for these applications.

Carbon/carbon and ceramic/ceramic composites have been considered for structural applications at temperatures above 1000°C. The availability and high specific strength and modulus of carbon/carbon composites are offset by their poor oxidation resistance. State-of-the-art coatings for carbon/carbon composites are susceptible to intermediate temperature oxidation and degradation by water vapor, making coated carbon/carbon composites high risk materials for applications requiring cyclical thermal and oxidative exposure. Ceramic/ceramic composites such as SiC/SiC_p have excellent inherent oxidation resistance, but are brittle over the entire application temperature range.

Metal-matrix composites based on refractory intermetallic compounds such as $MoSi_2$ are attractive alternatives to carbon/carbon and ceramic/ceramic composites because the intermetallic compounds are ductile at high temperatures while retaining good oxidation resistance. Silicide intermetallics are typically strong and brittle at low temperatures, strong and ductile just above the DBTT, and weak and ductile at high temperatures. A fundamental understanding of the mechanical behavior of the silicide matrix materials must be developed as a basis for designing silicide matrix composites that are tough at low temperatures and strong at high temperatures. In addition, extension of the fundamental concepts of composite reinforcements to the silicide-matrix systems will provide a scientific foundation for design and development of other intermetallic-matrix composites for applications above 1000°C.

2.0 RESEARCH APPROACH

The Achilles' heel of $MoSi_2$-based composites is their unacceptably low fracture toughness. Therefore, the focus of this research program was on improving the fracture toughness of $MoSi_2$ composites through ductile phase toughening and improved material processing.

In order to assess the stability of ductile phase tougheners in $MoSi_2$, a variety of refractory metal reinforcements were mixed with $MoSi_2$ powders and the reactions studied in detail. Ductile phase reinforcements with four different morphologies were used to make $MoSi_2$ composites and the composites were mechanically tested to determine fracture toughness at room temperature and bend strength at temperatures between room temperature and 1450°C. The fracture surfaces were analyzed and the toughness behavior was discussed within the framework of current theory.

The HIPing process was optimized to produce low porosity material with well-dispersed and properly arranged reinforcements. Along with empirical research to optimize the processing, theoretical work was performed to model the HIP process. The theoretical modeling was performed at Washington University and centered around developing HIP maps and deformation mechanism maps for $MoSi_2$ and $MoSi_2$ composites.

3.0 RESULTS

3.1 Processing

3.1.1 Description of Materials

The material used in this study was produced by hot isostatic pressing (HIPing) prealloyed powders. Prealloyed $MoSi_2$ powder was procured from four different sources:

Alfa Products, Danvers, MA; Aramco, Ossining, NY; Cerac, Inc., Milwaukee, WI; and Hermann Starck GmbH, Berlin FRG. The powders were screened for purity, stoichiometric accuracy, and powder particle uniformity. Based on these three criteria, the Cerac powder was determined to be the best and was used for the remainder of the program. The average Fe, Al, O, C, and N impurity concentrations for Cerac powder were determined by Analytical Associates, Detroit, MI, and are listed in Table 1.

Table 1. Impurity Concentrations in Cerac $MoSi_2$ Powder, wt%

Fe	Al	O	C	N
0.20	0.15	0.54	0.25	0.09

Material was also assayed after HIP consolidation, and no significant impurity pickup was detected. Typically, the material was slightly substoichiometric in Si content, averaging 35.7 wt% Si ($MoSi_2$ is 36.9 wt% Si ideally). Despite being substoichiometric, a significant amount of SiO_2 was observed in the HIPed Cerac material, as seen in Fig. 1.

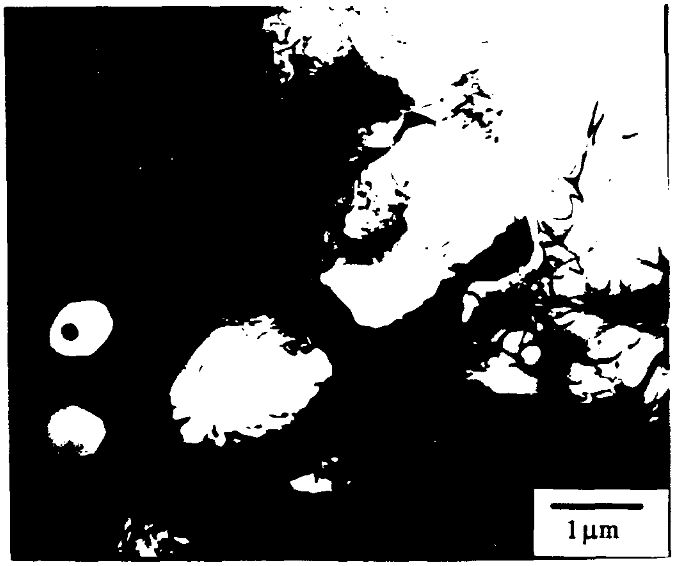

Figure 1. TEM micrograph of typical HIPed Cerac $MoSi_2$ powder, showing SiO_2 (light phase) and Mo_5Si_3 (dark phase).

Since $MoSi_2$ is a line compound, this Si deficit causes the Mo_5Si_3 phase to form, visible as the darkest phase in Fig. 1. The SiO_2 and Mo_5Si_3 content was typically ~ 2 vol%, and appears to be very difficult to altogether eliminate in HIPed powder material. The Cerac powder was nominally -325 mesh (< 44 μm diam.), and this powder size correlates well with the 10-50 μm grain diameters observed in the material after HIP consolidation.

3.1.2 General Procedures for HIP Consolidation

Powder was prepared for HIPing by canning the material in Nb containers. Care was taken to limit exposure of the $MoSi_2$ powder to air for prolonged periods during the canning process, and the powder was stored in Ar to limit oxidation. The powder filled cans were degassed for ~ 16 h in a 10^{-6} Torr vacuum, and sealed in vacuo. Specimens were HIPed using two different can geometries. The first was a simple 0.75 inch diam. Nb tube, crimped and electron beam welded on both ends. This type of can was convenient for monolithic and particle reinforced materials. The second geometry was a fabricated Nb pan, designed for producing fiber reinforced and laminated composite specimens. This can will be described in detail in Section 3.1.3. Both tube and pan type cans were capable of producing high-density, fully consolidated material.

HIPing was performed under 207 MPa isostatic pressure for a variety of temperatures and times. Early work in this program used 1700°C/4 h, which produced fully dense (> 97% of ideal density) material. However, this high temperature was detrimental to specimens containing reactive reinforcement materials, so lower temperatures were used in the latter phase of this program, typically in the 1200-1400°C range. These lower temperature HIPed materials showed far smaller reaction zones around the reactive reinforcements, as will be seen in section 3.3.2. It was found that slow cooling (< 5°C/min) under either full pressure (207 MPa), or slowly released pressure (~ 2 MPa/min) produced the best material. Excessively rapid cooling, or release of pressure at elevated temperatures appeared to result in microcracking in the consolidated composite material, as seen in a typical example in Fig. 2. A typical HIP temperature/pressure vs. time profile is shown in Fig. 3. Note that this profile was not strictly adhered to, and is shown only to give a general sense of the parameters used.

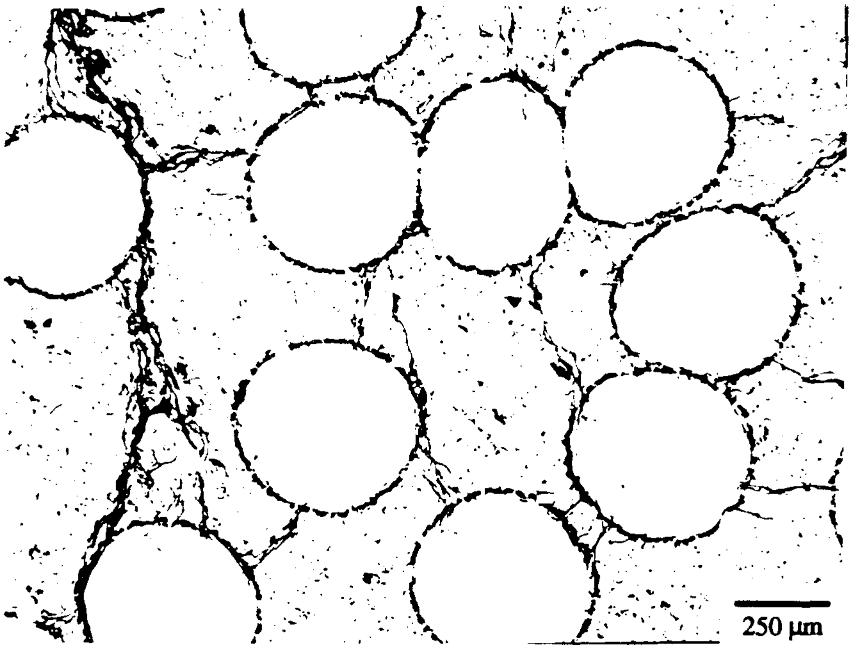

Figure 2. Optical micrograph of a Nb-wire reinforced $MoSi_2$ specimen, showing cracking due to pressure release at elevated temperature.

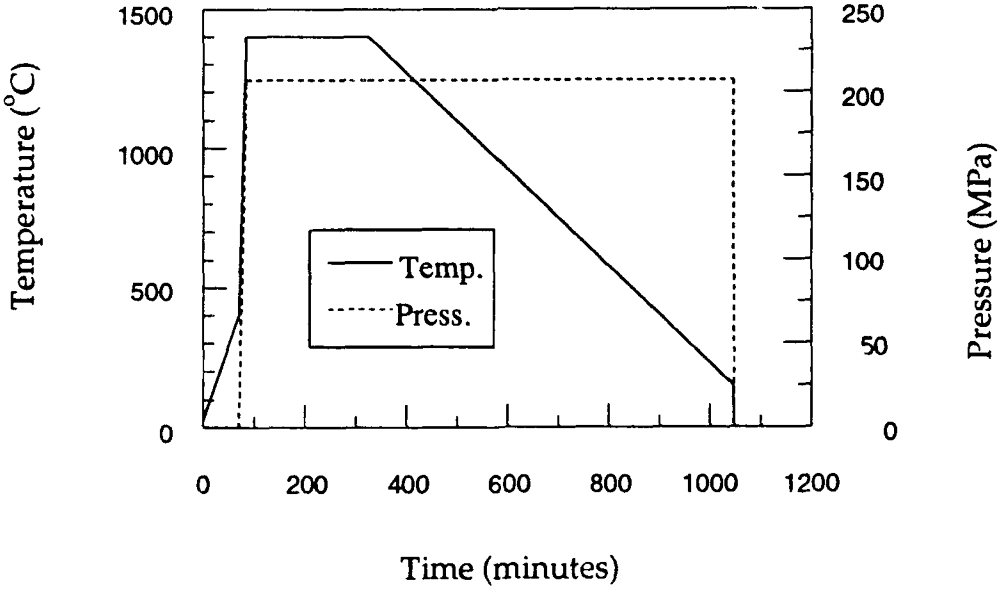

Figure 3. Typical HIP temperature (solid line)/pressure (dotted line) vs. time profile found to produce high quality composite material.

3.1.3 Description of Specialized Cans for Fiber Reinforced and Laminated Composites

Tubular HIP cans are not convenient for producing composite materials which require reinforcement lay-up, such as the Nb wire and Nb foil reinforced composites produced for this program. A more useful can was designed, and is shown schematically in Fig. 4. These cans consisted of a cylindrical 2 inch diameter x 0.5 inch deep pan cold drawn slightly off-center in a 3.5 x 4.5 x 0.02 inch Nb sheet. Powder and reinforcements were then layed-up in the pan with the appropriate arrangement. A 3.5 x 4.5 x 0.02 inch top plate was then seam welded onto the pan, along with a vacuum line sealed between plate and pan. The sealed pan was then pumped through the vacuum line to about 5×10^{-6} Torr. Finally, the vacuum line was welded shut, and the can was ready for HIPing. A drawback of this can design is the larger length of weld required, as compared to a tube-shaped can. This increases the chances for a leak, which results in a porous, sintered HIP product. Leaks were not found to be a major problem with the pans, and they generally performed well throughout this program. An additional benefit of the pan design is that 4-8 mechanical test specimens can be cut from the consolidated pan produced by a single HIP run, at least twice the yield of a typical 0.75 inch diam. tubular can.

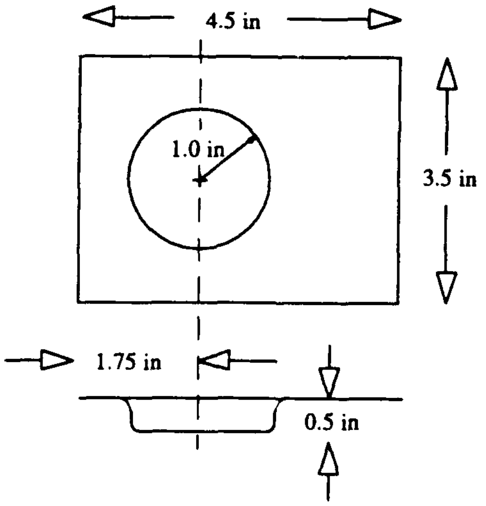

Figure 4. Schematic of pan-shaped can designed for HIPing fiber reinforced and laminated composites.

3.2 HIP Modeling

A systematic study was conducted to determine optimum pressure, temperature, and time parameters for HIP densification of monolithic $MoSi_2$, $MoSi_2$ reinforced with 20 vol% SiC whiskers, and $MoSi_2$ reinforced with 20 vol% Nb particulates. Samples were consolidated by HIP at three different temperatures, and two HIP times. Density measurements were performed by the weight loss (Archimedes Principle) method. A HIP map program was written based on the HIP densification models of Ashby and co-workers (Refs. 1-3) and the flow diagram suggested by Helle et al. (Ref. 3). The densification rate equations used in the program were the same as those used in the study by Schaefer (Ref. 4). Material data required for input to the programs were taken from literature or were estimated when published property data were not available. Data for composites that were not available in literature were calculated based on the rule-of-mixtures approach using the values for the constituents and their volume fractions or experimentally determined. The effects of error in the material data upon the HIP densification calculations is discussed in Section 3.2.6. The results of the program were compared with the experimentally determined data in Section 3.2.4.

3.2.1 Experimental Details

The $MoSi_2$ powder (-325 mesh, 99.5%) and the Nb powder (coarse: -80 +200 mesh, 99.8%; Fine: -325 mesh, 99.5%) were procured from Cerac, Inc., Milwaukee, WI; and the SiC whiskers (3:1 aspect ratio, wet-35% water mix) from Advanced Refractory Technologies (ART), Inc., Buffalo, NY. The SiC whiskers were dried prior to blending. In the case of composites, the matrix and reinforcement particles were mechanically blended for more than 12 hours. The powder was poured into Nb cans sealed on one end by TIG welding, degassed, and sealed on the other end by electron beam welding. The cans were then HIPed in an argon atmosphere at 207 MPa (30 ksi) pressure, three different temperatures (1200°C, 1300°C, 1400°C) and for two time intervals (52 min, 4 hrs) for each type of material under study.

Immersion density measurements were done on samples by the Archimedes principle method (Ref. 5). This technique determines density by measuring the difference in specimen mass in (a) air and (b) when suspended in a liquid of known density at a known temperature. The density is given by

$$D = \frac{\left(\frac{Wt_{air}}{Wt_{tol}} \bullet D_{tol} \right)}{\frac{Wt_{air}}{Wt_{tol}} - 1} \tag{1}$$

Where D_{tol} is the density of the liquid (in this case toluene), Wt_{air} is the weight in air, and Wt_{tol} is the weight in liquid. The density of the liquid as a function of temperature is given by:

$$D_{tol} = 0.8845 - 9.159 \bullet 10^{-4} T + 3.36 \bullet 10^{-7} T^2 \tag{2}$$

where T is in °C. The weight of the suspension wire was taken into account by a compensating weight. The CAHN 28/29 precision microbalance was used to measure the weight of samples in air and in toluene. The microbalance is sensitive to weight changes of less than ± 0.1 μg. The microbalance was interfaced with a computer which analyzed the weight data (taken at 7 s. interval, over a 1 hr. period) and reported the value with the minimum standard deviation. The toluene was contained in a glass petridish and the temperatures of the liquid was measured at regular intervals. The entire apparatus was located on an isolated table to minimize fluctuations in measurements.

3.2.2 Microstructural Characterization

Figures 5 and 6 show the decrease in porosity with temperature and time, respectively. The grain size variation and the change in pore morphology is also shown. Grain sizes in the monolithic case varied from 23 µm to 35 µm over the range of process conditions considered. For the Nb-reinforced composites the grain size variation was 28 µm to 36 µm. For the SiC reinforced material the grain sizes were in the range of 13.3 µm to 21.4 µm, which is lower by 10-15 µm than the base material. This difference

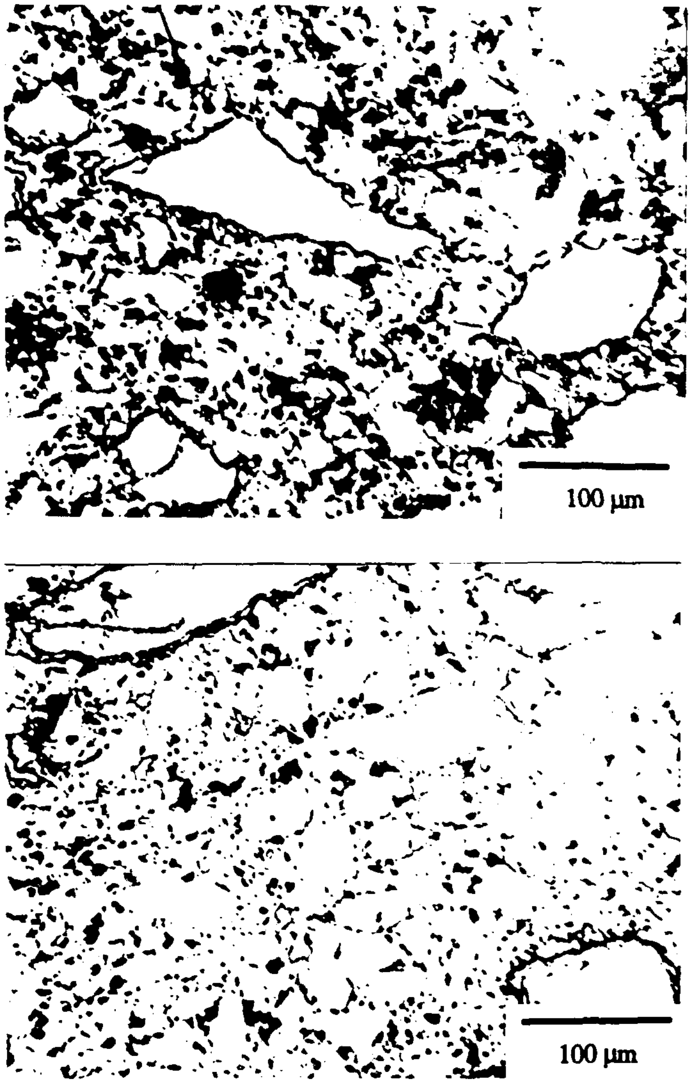

Figure 5. Decrease in porosity and increase in grain size with temperature for $MoSi_2$ + Nb powder composite. HIP conditions: (above) 1200°C/207 MPa/1 h, (below) 1300°C/207 MPa/1 h.

follows the same qualitative trend as observed by Bhattacharya and Petrovic (Ref. 6). However, the magnitude of the difference is lower in the present case compared to the earlier study, probably due to the lower consolidation temperatures used in the present study. In the case of monolithic $MoSi_2$ the grain size increase with temperature was of the order of ~ 7 µm and that with time was at most 3 µm. Similar grain size increases were observed for the other two materials. The absence

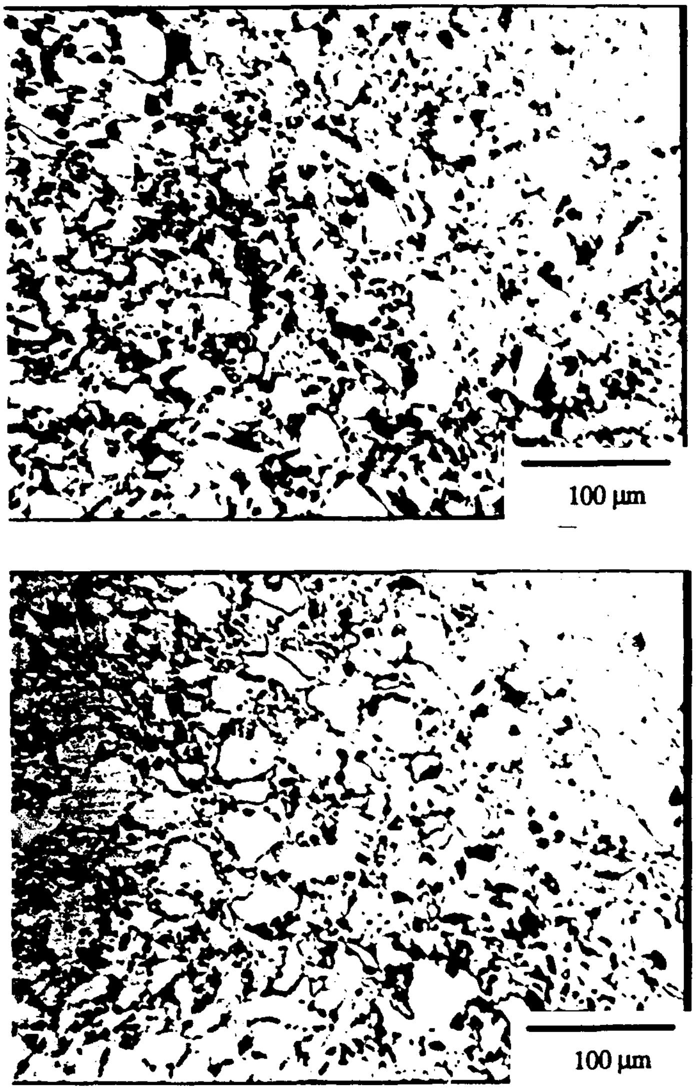

Figure 6. Decrease in porosity and increase in grain size with time for monolithic $MoSi_2$. HIP conditions: (above) 1200°C/207 MPa/1 h, (below) 1200°C/207 MPa/4 h.

of fine grains in the three consolidated materials suggests that diffusion is probably not the primary densification mechanism. The low diffusivities, especially of the metal atoms, reinforce the above observation.

Figures 5 and 6 also shows the pore morphology variation with respect to the consolidation conditions. At lower temperatures the pores are mostly irregular spheres, interspersed with some pores that are cusped shaped. At higher temperatures pores become more regular spherical in shape, especially in the case of materials consolidated at 1400°C. The pores are along prior powder particle or grain boundaries (since powder particle size and grain size are approximately equal). The cusp shaped porosity observed in the specimens consolidated at lower temperatures suggests a deformation based mass transport mechanism as opposed to a diffusion based mass transport. This, the observed grain sizes, and the low diffusivities of the constituents, suggests that densification is mostly likely dominated by PLC (Power Law Creep).

3.2.3 Creep of $MoSi_2$ and $MoSi_2$ Composites

Creep data for Nb reinforced $MoSi_2$ is not yet available in the literature. In order to get the PLC parameters of $MoSi_2$ + Nb required for the HIP Maps program compression creep tests were done on $MoSi_2$ + Nb samples. Since most creep data available for $MoSi_2$ and $MoSi_2$ + SiC materials were measured using materials processed by hot pressing, it was necessary to verify the creep results for the HIPed materials used in this study.

Test specimens of monolithic $MoSi_2$, $MoSi_2$ + Nb, and $MoSi_2$ + SiC were prepared by electrodischarge machining of the HIPed compacts, which were further cut by a diamond saw. These were tested in compression under constant load using SiC platens and rams. The displacement of the lower cross head of the MTS testing machine was recorded as a function of time. Only displacement curves that exhibited fairly straight lines were used in the analysis of data. The incremental load method was used once steady state was attained at a particular load. Tests were performed in the temperature range of 1100°C to 1300°C.

Figure 7 shows the steady state creep rate as a function of applied stress for the three materials at temperatures between 1100°C and 1300°C. The slopes of the regression fit lines (corresponding to the PLC exponents) are noted in the figure. The stress exponents are comparable to results of earlier studies on $MoSi_2$ and $MoSi_2$ + SiC (Refs. 7-13). The creep rates of $MoSi_2$ + Nb are higher at both temperatures compared to the

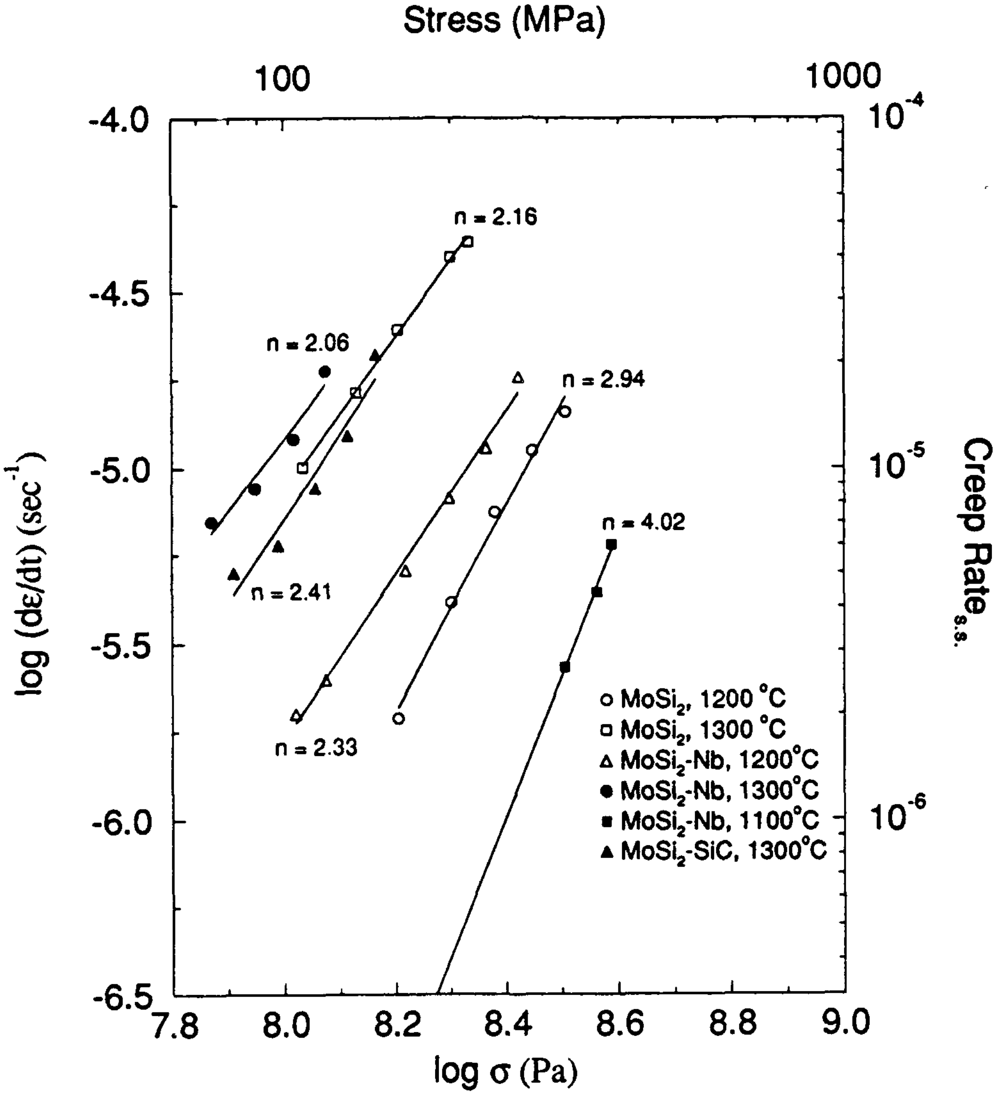

Figure 7. Steady state creep rate as a function of applied stress for $MoSi_2$, $MoSi_2$ + Nb, and $MoSi_2$ + SiC.

monolithic case. The creep rates of $MoSi_2$ + SiC measured here are only slightly lower than the monolithic material. This small difference in creep rates is contrary to the significantly lower creep rates obtained for $MoSi_2$ + SiC in earlier studies. One possible explanation for this discrepancy is the low density of the $MoSi_2$ + SiC specimen, approximately 96%, compared to the nearly fully dense specimens used by earlier workers. Also, the much smaller grain sizes in the SiC reinforced case may enhance the kinetics of Mo diffusion in $MoSi_2$, which is thought to be the rate controlling step in the kinetics of creep of $MoSi_2$ (Ref. 8), and may lead to higher creep rates. The average creep exponents for $MoSi_2$, $MoSi_2$ + Nb, and $MoSi_2$ + SiC in the 1200°C-1300°C temperature range are 2.2, 2.55, and 2.41, respectively. The exponent for the Nb reinforced material varies from 2.06 at 1300°C to 4.02 at 1100°C. This increase in the value of n with a decrease in temperature is expected for metallic materials. A plot of the steady state creep rate versus inverse absolute temperature is shown in Fig. 8. From this data an activation energy of 160 kJ/mol is calculated for the $MoSi_2$ + Nb material.

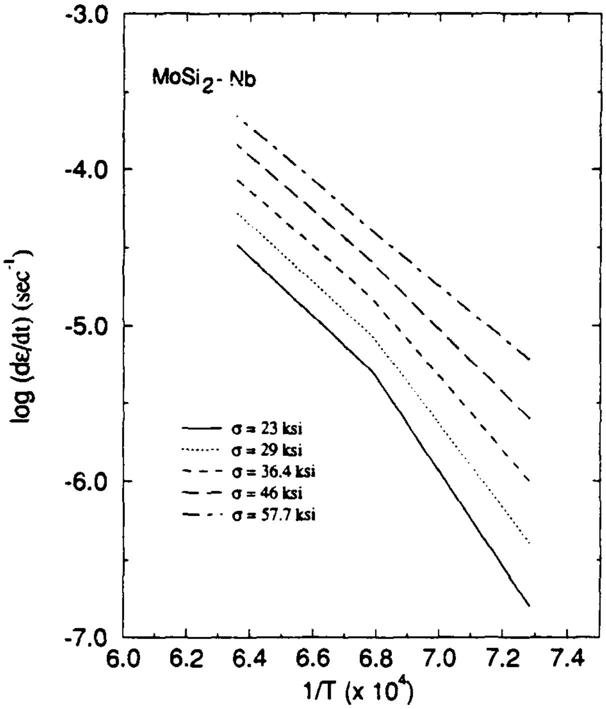

Figure 8. Steady state creep rate as a function of inverse absolute temperature for $MoSi_2$ + Nb at five stress levels.

3.2.4 Comparison Between Model Results and Measurements

The measured relative density data along with the consolidation conditions for each of the materials considered in this study is shown in Table 2. As discussed by Ashby and co-workers (Refs. 1-3) the HIP Map is based on the rate equations for the various densification mechanisms (plastic yielding, power law creep, boundary diffusion, volume diffusion, surface diffusion, pipe diffusion, grain boundary sliding, etc.) operative during the process. The rate equations are listed in Section 3.2.6. The mechanisms are assumed to operate in parallel and, therefore, the net densification rate is given by the sum of the rates due to each mechanism. Each mechanism is described by a set of two equations, one for the earlier stage of interconnected porosity and the other for the later

Table 2. Measured Relative Density Data and Consolidation Conditions for the Materials in the Study. Pressure = 207 MPa,
f: Fine Niobium; c: Coarse Niobium Powder

Sample Number	Temperature (°C)	Time (hrs.)	Relative Density
$MoSi_2$, monolithic			
1	1200	0.87	0.880
2	1300	0.87	0.944
3	1400	0.87	0.983
4	1200	4.0	0.928
5	1300	4.0	0.965
6	1400	4.0	0.986
$MoSi_2$ + 20 vol% Nb particles			
7	1200	0.87	0.934^c
8	1300	0.87	0.948^c
9	1400	0.87	0.971^c
10	1200	4.0	0.966^f
11	1300	4.0	0.970^f
12	1400	4.0	0.977^f
$MoSi_2$ + 20 vol% SiC whiskers			
13	1200	0.87	0.772
14	1300	0.87	0.906
15	1400	0.87	0.932
16	1200	4.0	0.903
17	1300	4.0	0.945
18	1400	4.0	0.960

stage (> 95% density) of isolated porosity. The net densification rate is integrated to get the constant time contours in a relative density versus temperature or pressure plot. The boundary between the region of dominance of any two mechanisms is determined by equating the densification rate equation for the particular two mechanisms.

Figure 9 shows the relative density (ρ) versus temperature (in Kelvin) HIP Map for the three materials considered in this study. Earlier studies used HIP temperatures of

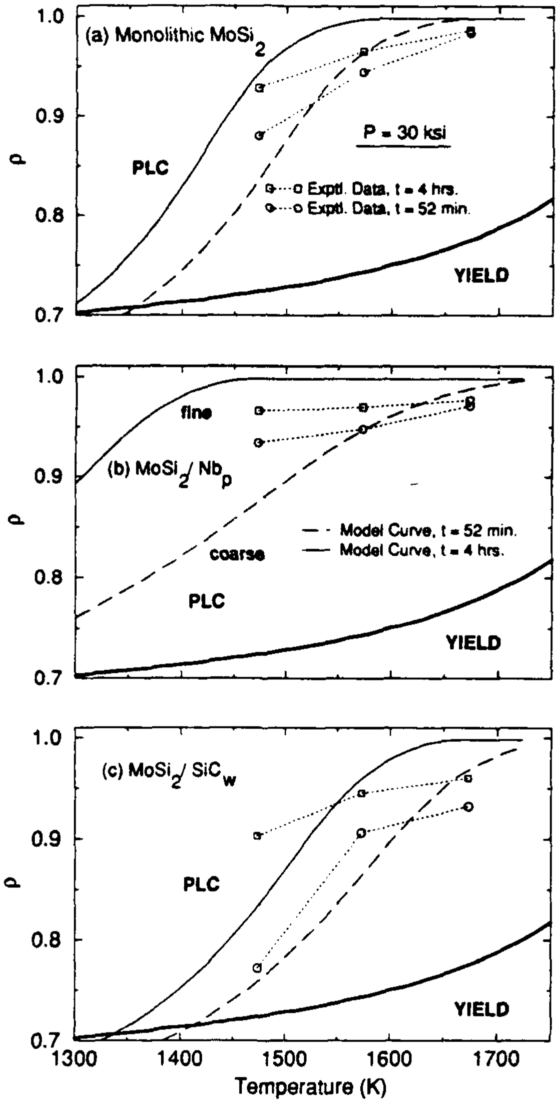

Figure 9. HIP densification diagram for (a) $MoSi_2$, (b) $MoSi_2$ + 20 vol% Nb (fine Nb: 45 μm diam, coarse Nb: 62 μm diam), and (c) $MoSi_2$ + 20 vol% SiC. The pressure is constant at 207 MPa, and the thick lines represent boundaries between two different densification mechanisms, plastic yielding, and PLC.

1600-1700°C at pressures close to 207 MPa and HIP times of about 4 hrs. (Refs. 14, 15). The results in Table 2 show that very close to full density can be achieved at lower temperatures or pressures than used in earlier studies. Even though the error in prediction seems to be considerable, the magnitudes of error are similar to earlier studies on other materials (Refs. 16-18). Also, the accuracy of the HIP map is significantly dependent on the precision with which the material property values are known. It has been shown that typically expected variations in material property data introduce considerable uncertainty in the model predictions (see Section 3.2.6).

The accuracy of the experimental data is also affected by several other factors. The values for the density of the fully dense materials in all three cases was taken to be the value corresponding to their pure state which is somewhat different than the density of commercial material. The precision microbalance used to measure mass of the samples is fairly accurate, as mentioned earlier, but the taring and calibration procedures introduce a certain amount of error in the measured data.

3.2.4.1. Monolithic $MoSi_2$

The values of the material properties for $MoSi_2$ used in the HIP maps program are listed in Table 3 (Refs., 8,15,19,20). The pre-exponent for volume diffusion for $MoSi_2$ was not available in the literature. The diffusion of silicon in $MoSi_2$ has been studied (Ref. 21) but the diffusion of molybdenum in $MoSi_2$, which is small compared to silicon (Ref. 8,22) - has not yet been documented. The value used in this study was estimated so as to give a better fit with the experimental data. The other approximations used to determine diffusivity data are according to Frost and Ashby (Ref. 23) and have been listed at the end of Table 3. Superscripts on the values in Table 3 indicate the method used to estimate the value of the material property data. Figure 9(a) shows the HIP diagram for base $MoSi_2$. The constant time curves are for 52 minutes and 4 hrs. The

Table 3. Input Material Property Data for $MoSi_2$, $MoSi_2$ + 20 vol% Nb_p, and $MoSi_2$ + 20 vol% SiC_w

Material Property	$MoSi_2$	Ref.	$MoSi_2/Nb_p$	Ref.	$MoSi_2/SiC_w$	Ref.
Crystallographic Data						
Atomic Vol. (m^3)	8.06E-29	19	8.06E-29$^{(5)}$		8.06E-29$^{(5)}$	
Burgers Vector (m)	4.53E-10	19	4.53E-10$^{(5)}$		4.53E-10$^{(5)}$	
Thermal Data						
Melting Temp (K)	2303	19	2303$^{(5)}$		2303$^{(5)}$	
Mechanical Property Data						
Shear Modulus at 300K, μ_o (MPa)	1.63E05	20	1.4E11$^{(3)}$		19$^{(4)}$	
Temp. Dependence, $\frac{T_m}{\mu_o}\bullet\frac{d\mu}{dT}$	-0.35$^{(4)}$		-0.28$^{(3)}$		-0.35$^{(5)}$	
Yield Stress at 0 K (MPa)	2344	15	2137	15	2827	8
Temp. Dependence, $\frac{T_m}{\sigma_{yo}}\bullet\frac{d\sigma_y}{dT}$	-1.29	15	-1.32	15	-1.37	8
Lattice Diffusion						
Pre-exponent (m^2/sec)	2.0E-06$^{(4)}$		3E-10$^{(3)}$		1.5E-02$^{(4)}$	
Act. Energy (kJ/mol)	380$^{(1)}$		160$^{(1)}$		460$^{(1)}$	
Boundary Diffusion						
Pre-exponent (m^3/sec)	1.81E-15$^{(2)}$		2.72E-19$^{(2)}$		1.35E-11$^{(2)}$	
Act. Energy (kJ/mol)	244$^{(1)}$		105.6$^{(1)}$		300$^{(1)}$	
Core Diffusion						
Pre-exponent (m^4/sec)	1E-23$^{(4)}$		4E-21$^{(2)}$		2.5E-19$^{(2)}$	
Activation Energy (kJ/mol)	244$^{(1)}$		253$^{(1)}$		300$^{(1)}$	
Power Law Creep						
Exponent	1.75	8	2.2		2.631	8
Activation Energy (kJ/mol)	380	8	160		460	8
Reference Stress (MPa)	14	8	80.4		35	8
Reference Temp. (C)	1300		1200		1400	
Dorn's Constant, A	4.432E04	8	3.04E-05		1.93E04	8
Obstacle Controlled Glide						
0 K flow stress, τ/μ_o	0.01$^{(4)}$		0.01$^{(3)}$		0.01$^{(4)}$	
Pre-exponent, γ_o (sec^{-1})	1E06$^{(4)}$		1E06$^{(4)}$		1E06$^{(4)}$	
Activation Energy, $\Delta F/\mu_o b^3$	0.5$^{(4)}$		0.5$^{(4)}$		0.5$^{(4)}$	
Lattice Resistance Controlled Glide						
0 K flow stress, τ/μ_o	0.05$^{(4)}$		0.0434$^{(4)}$		0.05$^{(4)}$	
Pre-exponent, γ_p (sec^{-1})	1E11$^{(4)}$		1E11$^{(4)}$		1E11$^{(4)}$	
Activation Energy, $\Delta F_p/\mu_o b^3$	0.05$^{(4)}$		0.06$^{(3)}$		0.05$^{(4)}$	
Physical Property Data						
Material Density (g/cc)	6.24		6.706		5.634	
Initial Relative Density	0.64		0.64		0.064	
Ave. Particle Radii (µm)	22.5		22.5 (fine), 30.75 (coarse)		28	
Ave. Grain Size (µm)	30		30		18	

(1) $Q_{vol} \simeq Q_{PLC}$; $Q_{bdry} \simeq 0.66 \bullet Q_{vol}$; $Q_c \simeq Q_{bdry}$ (Ref. 31) (2) $\delta D_{obdry,\ vol} \simeq 2 \bullet b \bullet D_{obdry,\ vol}$ (Ref. 31); $a_c D_{oc} \simeq 4 \bullet b \bullet \delta D_{obdry}$ (3) Estimated by Rule-of-Mixtures approach (4) Estimated to get better agreement with data (5) Assumed equal to matrix value

map is drawn for an average particle size of 45 μm (which corresponds to a mesh size of -325) and an average grain size of 30 μm. The model predicts full densification at ~ 1600°K with a pressure of 207 MPa and HIP time of 4 hrs. In the temperature range considered, the model predicts PLC to be the dominant densification mechanism. The thick line in Fig. 9(a) shows the boundary between plastic yielding and PLC. The temperature range 1200°C to 1400°C exhibits a considerable drop in the value of yield stress (see Section 3.4.3.1). In the present study the temperature dependence of yield stress has been approximated as constant, as done in earlier studies of this nature. The compressive yield strength versus temperature data of Soboyejo et al. (Ref. 15) was extrapolated to get the yield stress at 0°K and the temperature dependence of yield stress. There is general agreement between the model predictions and the experimental data, although the model predicts a steeper increase in relative density than experimentally observed. In summary, at 207 MPa (30 ksi) pressure and HIP times of around one to four hours, the temperature required to achieve densification of ~ 98.5% by HIP has been found to be in the 1400°C-1500°C range, compared to temperatures close to 1700°C used in earlier studies on the HIP of $MoSi_2$ based materials.

3.2.4.2 $MoSi_2$ + 20 vol% Nb_p

Some of the material property data for niobium particulate reinforced composites were calculated based on the rule-of-mixture approach and are shown in Table 3. The material property data for pure Nb was taken from Frost and Ashby (Ref. 23). Data on temperature variation of compressive yield stress (Ref. 15) was used to extrapolate the yield stress properties required. Results of the compression creep tests at 1200°C and 1300°C on the most dense $MoSi_2$ + Nb sample (see Section 3.2.3) gave the values for the PLC properties used in the HIP Maps program. The constant time contours for 52 minutes and 4 hours were drawn with the values of average particle radii as 30.75 and 22.5 μm, respectively. The HIP diagram is shown in Fig. 9(b). Comparison of the experimental curves in Figs. 9(a) and 9(b) shows that at the same pressure and temperature conditions the Nb reinforced composite densifies in less time than the unreinforced matrix. This is in agreement with the observations of Li and Funkenbusch (Ref. 24). However, in the final stages of densification the Nb reinforced material experiences a retardation in densification. The difference in the experimental curves for the case of base $MoSi_2$ and $MoSi_2$ + 20 vol% Nb_p is not significant, the 20 vol% reinforcement producing only a small shift in the HIP densification curves. Therefore, the rule-of-mixtures approach for the determination of some of the data in Table 3 for the composites can be used as a first approximation, even though this approach does not have a firm theoretical basis. The average grain size value of 30 µm and an average particle size of 45 µm was used for the construction of Fig. 9 (b). The model predicts higher relative density than experimentally determined at relative densities > 0.95. The dominant densification mechanism is PLC, as in the case of the unreinforced matrix.

3.2.4.3 $MoSi_2$ + 20 vol% SiC_w

The density versus temperature HIP densification diagram for $MoSi_2$ + 20 vol% SiC is shown in Fig. 9(c). The input data for this material is shown in Table 3. The yield stress data required for the construction of the domain boundaries was extrapolated from the data of Petrovic and Honnell (Ref. 25). The values of particle radii and grain size used to construct this map are 28 µm and 18 µm, respectively. The agreement with experimental data seems to be better than in the earlier two cases. The dominant densification mechanism, as in both earlier cases, is PLC. Besson and Evans (Ref. 26) have suggested that densification is strongly inhibited by high aspect ratio, non-deformable reinforcements, probably due to flow constraints. This is in agreement with the strikingly large difference in densification between $MoSi_2$ and $MoSi_2$ + SiC_w.

3.2.5 Deformation Mechanism Maps for $MoSi_2$ and $MoSi_2$ Composites

This section describes modeling of the plastic deformation of $MoSi_2$ and its composites, and the construction of the deformation mechanism maps originally developed by Ashby and Frost (Ref. 23).

3.2.5.1 Deformation Mechanisms and Rate Equations

The deformation mechanisms considered in this study were:

1. Collapse at ideal strength
2. Plasticity by dislocation glide
3. Power law creep by dislocation glide, or glide plus climb
4. Diffusional flow

Plastic flow in fully dense solids is caused by the shearing, or deviatoric part of the stress field, σ_S. This shear stress nucleates and exerts forces on defects - dislocations, vacancies, etc., - causing them to move and the material to deform plastically. The shear strain rate, $\dot{\gamma}$, reflects the density, mobility, and potency of deformation carriers. Each mechanism of deformation can be described by a rate equation which relates $\dot{\gamma}$ to the stress σ_S, the temperature T, and to the structure of the material at that instant:

$$\dot{\gamma} = f(\sigma_s, T, M_i, N_i) \tag{3}$$

where M_i and N_i are the material properties and the microstructural variables, respectively, which describe the structure of the material. In this study, the M_i and N_i variables are assumed to be constant over the range of stresses and temperatures used, so the equation reduces to

$$\dot{\gamma} = f(\sigma_s, T). \tag{4}$$

3.2.5.2 Construction of Deformation Mechanism Maps

It is useful to have, for a polycrystalline solid, information about the range of dominance of each mechanism of plasticity, and the rates of flow they produce. This information is commonly displayed graphically using a deformation mechanism map (DMM, Ref. 23). Figures 10-12 are DMMs for $MoSi_2$, $MoSi_2$ + Nb, and $MoSi_2$ + SiC, respectively. The DMMs plot normalized stress, i.e., the applied stress divided by the shear modulus of the material, as a function of homologous temperature. Multiple contours are typically plotted on a single DMM, showing how stress vs. temperature varies with shear strain rate (each contour represents a 10 fold strain rate increase from left to right in Figs. 10-12). The thick lines on the DMMs demark the stress vs. temperature domains over which diffusion, PLC, or dislocation glide induced plasticity are the dominant deformation mechanism. However, all mechanisms are allowed to act simultaneously even in stress-temperature domains where they are not the dominant deformation mechanism. Therefore the DMMs actually plot contours of equal <u>net</u> shear strain rate as a function of stress and temperature, where the shear strain rates due to five independently acting deformation mechanism are summed together.

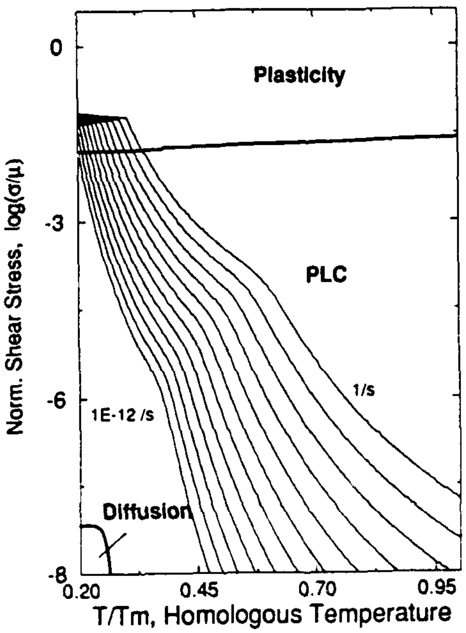

Figure 10. A stress-temperature map for $MoSi_2$ with a grain size of 30 μm.

The net strain rate of a polycrystal subjected to a stress σ_S at a temperature T is:

$$\dot{\gamma}_{net} = \dot{\gamma}_1 + \text{ greatest of } (\text{the least of } \{\dot{\gamma}_2, \dot{\gamma}_3\}, \dot{\gamma}_4) + \dot{\gamma}_5 \qquad (5)$$

where the subscripts 1 through 5 are, respectively, the strain rate due to elastic collapse, discrete obstacle controlled plasticity, plasticity limited by a lattice resistance, power law creep, and diffusional flow. The contours of constant strain rate are obtained by solving the above equation for σ_S as a function of T at a constant $\dot{\gamma}$. The domain boundaries shown as heavy lines in Figs. 10-12 are the loci of points at which two mechanisms contribute equally to the overall strain rate, and are computed by equating two pairs of rate equations, and solving for stress as a function of temperature. The rate equations used in this study are listed below.

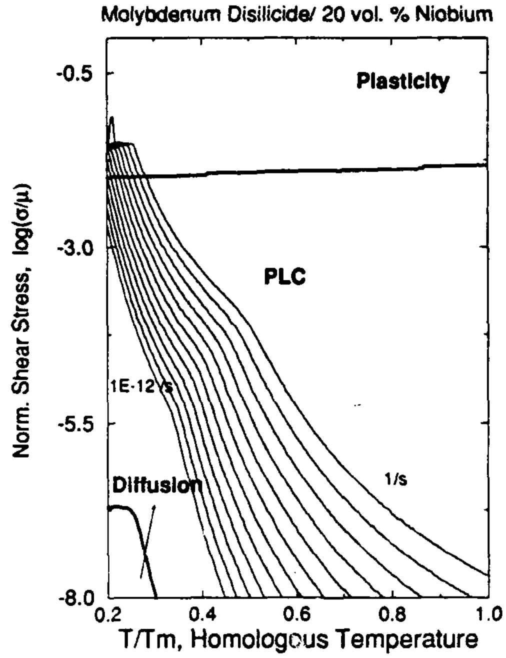

Figure 11. A stress-temperature map for MoSi2 + 20 vol% Nb with a grain size of 30 μm.

Discrete obstacle controlled plasticity:

$$\dot{\gamma} = \dot{\gamma}_o \exp\left[-\frac{\Delta F}{kT}\left(1-\frac{\sigma_s}{\tau}\right)\right] \tag{6}$$

Plasticity limited by lattice resistance:

$$\dot{\gamma} = \dot{\gamma}_p \left(\frac{\sigma_s}{\mu}\right)^2 \exp\left\{-\frac{\Delta F_p}{kT}\left[1-\left(\frac{\sigma_s}{\tau_p}\right)^{3/4}\right]^{4/3}\right\} \tag{7}$$

Power law creep:

$$\dot{\gamma} = \frac{A\mu b}{kT}\left(\frac{\sigma_s}{\mu}\right)^n\left[D_v + \frac{10a_c D_c}{b^2}\left(\frac{\sigma_s}{\mu}\right)^2\right] \tag{8}$$

Diffusional flow:

$$\dot{\gamma} = \frac{42\sigma_s\Omega}{kTd^2}\left[1+\frac{\pi\delta D_b}{dD_v}\right] \tag{9}$$

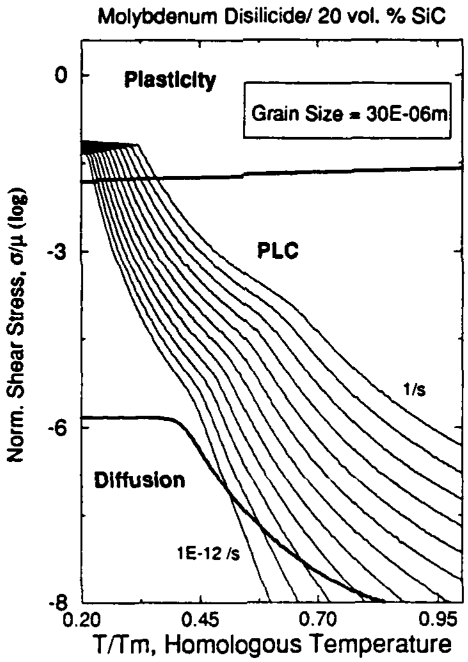

Figure 12. A stress-temperature map for $MoSi_2$ + 20 vol% SiC with a grain size of 30 µm.

constants are as follows:

A = Dorn's constant; $\dot{\gamma}$ = shear strain rate, σ_s = applied stress; μ = shear modulus; a_c = dislocation core radius; D_c = dislocation core diffusivity; τ = athermal flow strength; τ_p = flow stress at 0 K; ΔF = activation energy required to overcome obstacle; ΔF_p = Helmholtz free energy of an isolated pair of kinks; T = absolute temperature; b = Burgers vector; D_v = volume diffusivity; Ω = atomic volume; d = grain size; δ = grain boundary width; and D_b = grain boundary diffusivity.

The material property data used to construct the deformation maps for $MoSi_2$ and its composites are in Table 3. As in the case of the construction of the HIP maps many of the data have been estimated. In the case of $MoSi_2$ + Nb, many have been computed using the rule-of-mixtures approach.

3.2.6 Sensitivity Analysis of HIP Modeling

Some of the material property data values had to be estimated, due to lack of literature information, especially the values of the pre-exponents of diffusivities. Also, in certain cases empirical/semi-empirical relationships were used to determine the values of some material properties (listed under Table 3). The model predictions could be significantly affected by the accuracy with which the material property data values are known. A mathematical study was conducted to account for the error induced in the model predictions due to uncertainty in material property data values. The material property data for Ti-50 at.% Al has been documented in the literature, and detailed HIP studies have been done with the TiAl system (Ref. 16). Therefore, TiAl was used as the material system to conduct the mathematical analysis. The analysis is quite general, however, and can be applied to the $MoSi_2$ system as well. The following is a description of the analysis.

It has been acknowledged by the developers of HIP maps that the accuracy of the predictions is limited by the precision with which material property data, used in the HIP maps program (Ref. 27), are known. In many cases, these data are known, at best, to within a factor of two (Ref. 3). A few examples to elucidate this follow. Boundary diffusion is the dominant densification mechanism during the HIP of Alumina (Refs. 2,3). The material properties with regard to this mechanism are the pre-exponent for boundary diffusion, which is the grain boundary diffusion coefficient times the grain boundary width (δD_{ob}), and the activation energy (Q_b). Frost and Ashby (Ref. 23) reported a value of $8.6 \times 10^{-10} m^3/s$ for δD_{ob} and 419 kJ/mol for Q_b. In a more recent study, Uematsu et al. (Ref. 28) reported a value of $3.3 \times 10^{-11} m^3/s$ and 390 kJ/mol, respectively, for the two material properties at the typical HIP temperature conditions. Larger discrepancies in the values of boundary diffusion constants (approximately three orders of magnitude difference in the value of δD_{ob}) have been reported by Kim et al. (Ref. 29) in their paper on the HIP of Y-TZP powders compared to a similar study by Oishi et al. (Ref. 30). In the case of TiAl, power law creep (PLC) is the dominant mechanism and the power law exponent (n), the activation energy (Q_{plc}), and the reference stress for PLC (σ_{ref}), are the controlling parameters. Martin et al. (Ref. 31) reported a value of 4 for n and 300 kJ/mol for Q_{plc} compared to the values used by Choi et al. (Ref. 16) of 3 and 320 kJ/mol, respectively. Kampe et al. (Ref. 32) reported an even higher value for Q_{plc} (340 kJ/mol) and a value of 1.9 to 2.3 for n. Hayes and London (Ref. 33) reported values of 326.4 kJ/mol and 4.95 for Q_{plc} and n, respectively. Creep properties of TiAl alloys have been found to vary considerably due to differences in alloy compositions (Refs. 32,34,35), heat treatments (Ref. 32), and processing routes (Refs. 32,36). Even for materials processed similarly, there are typically variations in the values of material properties due to the inherent inaccuracies in the methods used to determine these properties. Such variations significantly affect the accuracy of the HIP model predictions. The effect of variations in the values of material properties on the HIP model predictions was determined by performing a sensitivity analysis with respect to material property data.

The values for material property data used in the HIP maps program are typically determined in one of the following ways: (a) experimental measurements at consolidation conditions; (b) estimates based on data on other materials; (c) back calculations using the experimentally determined HIP data; and (d) extrapolations to get appropriate material property values for the consolidation conditions. Methods other than (a) could result in the determination of a material property value which is highly unrealistic. For example, in the Kim et al. study (Ref. 29), the discrepancy in the values of boundary diffusion constants compared to Ref. 30 was attributed to the use of extrapolation of data [method (d)] in the earlier study. The present study discusses this with respect to a recent experimental study (Ref. 16) on TiAl and resolves the discrepancy by using PLC material parameters determined experimentally for conditions close to the actual HIP process conditions.

The sensitivity analysis primarily involves the calculation of a normalized sensitivity parameter, S_M, for the density with respect to a material property, M. We start from the densification rate equation during HIP, given by:

$$\dot{\rho} = \dot{\rho}_1 + \dot{\rho}_2 + \dot{\rho}_3 + \dot{\rho}_4 \ldots \qquad (10)$$

where the subscripts correspond to different transport mechanisms occurring during hot isostatic consolidation of powders. The densification rate equations used in the HIP modeling of $MoSi_2$ are described below:

Volume Diffusion:

$$\dot{\rho}_1 = \frac{D_v P\Omega}{r^2 kT}\left\{43C(1-\rho_o)S_1 + 270(1-\rho)^{1/2}\left[\frac{1-\rho}{6}\right]^{1/3} S_2\right\} \qquad (11)$$

Boundary Diffusion:

$$\dot{\rho}_2 = \frac{\delta D_b P\Omega}{r^3 kT}\left\{43C^2 S_1 + 270(1-\rho)^{1/2} S_2\right\} \qquad (12)$$

Power law creep (PLC):

$$\dot{\rho}_3 = D_{PLC}\left(\frac{P}{\sigma_{ref}}\right)^n S_1 + 1.5\rho\left[\frac{1.5}{n(1-(1-\rho)^{1/n})}\right]^n S_2 \tag{13}$$

Nabarro-Herring Creep:

$$\dot{\rho}_4 = \left[\frac{D_v}{d^2} + \frac{\pi\delta D_b}{d^3}\right]\left[\frac{P\Omega}{kT}\right] \bullet \left\{14.4\frac{C^{1/2}}{\rho}S_1 + 32(1-\rho)S_2\right\} \tag{14}$$

where

$$C = \left(\frac{1-\rho_o}{\rho-\rho_o}\right)$$

$$S_1 = 1 - e^{-\left(\frac{1-\rho}{0.1}\right)^2}$$

$$S_2 = 1 - S_1$$

$$D_v = D_{o_v}\exp\left\{\frac{-Q_v}{RT}\right\}$$

$$D_b = D_{o_b}\exp\left\{\frac{-Q_b}{RT}\right\} \quad .$$

The constants are defined as follows:

ρ = relative density (density/ideal density), ρ_0 = initial relative density, D_v = volume diffusion coefficient, Ω = atomic volume, r = particle radii, k = Boltzman constant, T = temperature, D_b = boundary diffusion coefficient, δ = boundary thickness, P = pressure, D_{PLC} = power law creep diffusional parameter, σ_{ref} = reference stress power law creep, n = power law exponent, d = grain size in particle, $D_{o_{v,b}}$ = pre-exponent volume/boundary diffusion, $Q_{v,b}$ = activation energy volume/boundary diffusion, R = gas constant.

Differentiation of both sides of Eq. (10) with respect to the variable M results in a second order differential equation, which can be solved approximately for $\partial\rho / \partial M$, using the mean-value theorem for integrals. This differential term can be normalized to obtain the sensitivity parameter for relative density with respect to M, defined as:

$$S_{\rho M} = \frac{\partial \rho}{\partial M} \bullet \frac{M}{\rho} = \left(\frac{\frac{\partial \rho}{\rho}}{\frac{\partial M}{M}} \right) \qquad (15)$$

The sensitivity parameters for TiAl, with respect to PLC exponent (n), PLC reference stress (σ_{ref}), PLC activation energy (Q_{plc}), pre-exponent for boundary diffusion (δD_{ob}), and the activation energy for boundary diffusion (Q_b), plotted as a function of time at a constant pressure of 182 MPa and for three temperature conditions (1100°C, 1150°C, and 1200°C) are shown in Fig. 13. The calculation of the sensitivity parameter involves the

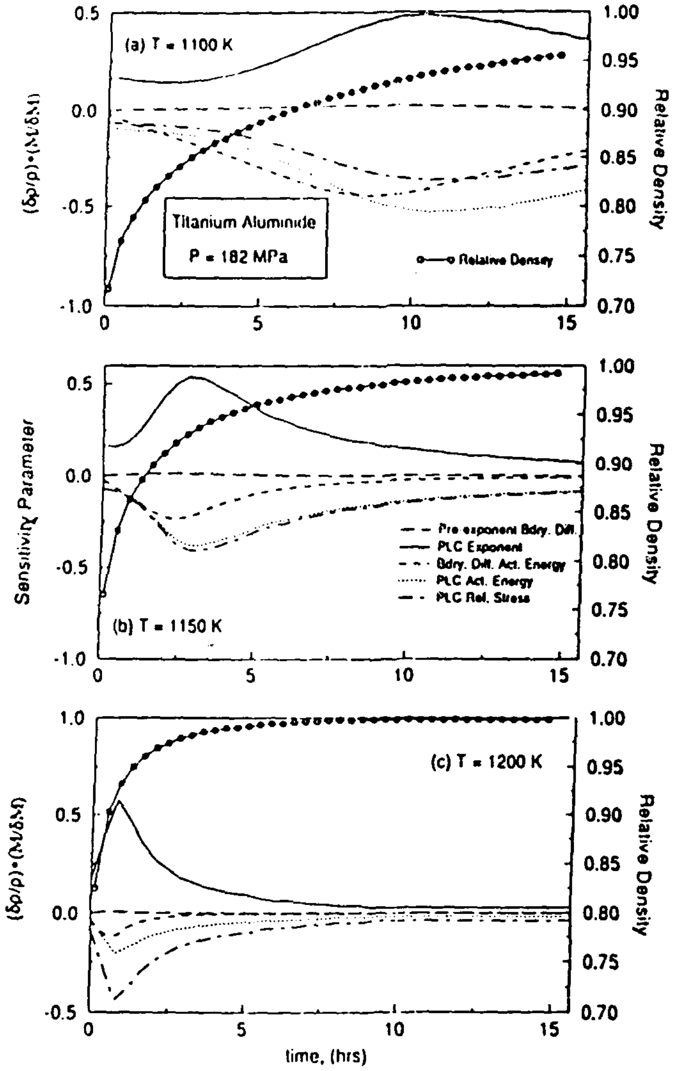

Figure 13. Sensitivity parameter for relative density, ρ, with respect to PLC and grain boundary diffusion material properties.

use of a mean value for M, values of which are listed in Table 4 for the different material properties considered. We find that for the temperature and pressure conditions considered, δD_{ob} has a negligible effect on the density predictions, whereas the PLC parameters, n and σ_{ref}, play a significant role and if their values were in error initially, we can expect considerable error in the density predictions. Also, in the region of relative densities of 0.87 to 0.95, where a change in the densification mechanism from PLC-I to PLC-II occurs (Ref. 16), the error in density predictions due to an error in the estimation of a material property value is significant. It can be observed that the sensitivity to PLC parameters is, in general, greater than that for the boundary diffusion parameters. This is expected, since PLC is the dominant mechanism in the densification of TiAl particulates at the temperature and pressures typically used for HIP consolidation. Equation (15) can also be used to determine the sensitivity of the densification rate with respect to the material property values. A similar mathematical analysis allows us to determine the sensitivity of densification rate with respect to a material property M, defined as:

Table 4. Mean Values and Variations About Their Mean Values for Material Property Data

Matl. Prop.	Q_{plc} (kJ/mol)	Q_b (kJ/mol)	σ_{ref} (MPa)	δD_{ob}(m^3/s)	n
M_{mean}	320	180	27	7.6×10^{-13}	3.00
ΔM	10	10	5	1.26×10^{-13}	0.5
$\Delta M/M_{mean}$ (%)	3.0	5.6	18.5	16.6	16.7

$$S_{\dot{\rho}M} = \frac{M}{\dot{\rho}} \bullet \frac{\partial \dot{\rho}}{\partial M} \qquad (16)$$

These calculations also involve the use of a mean value for the material property under consideration and are the same as in the previous analysis (Table 4). The bar charts shown in Fig. 14 show the sensitivity parameter for the densification rate with respect to the PLC and boundary diffusion parameters. The sensitivity analysis helps in

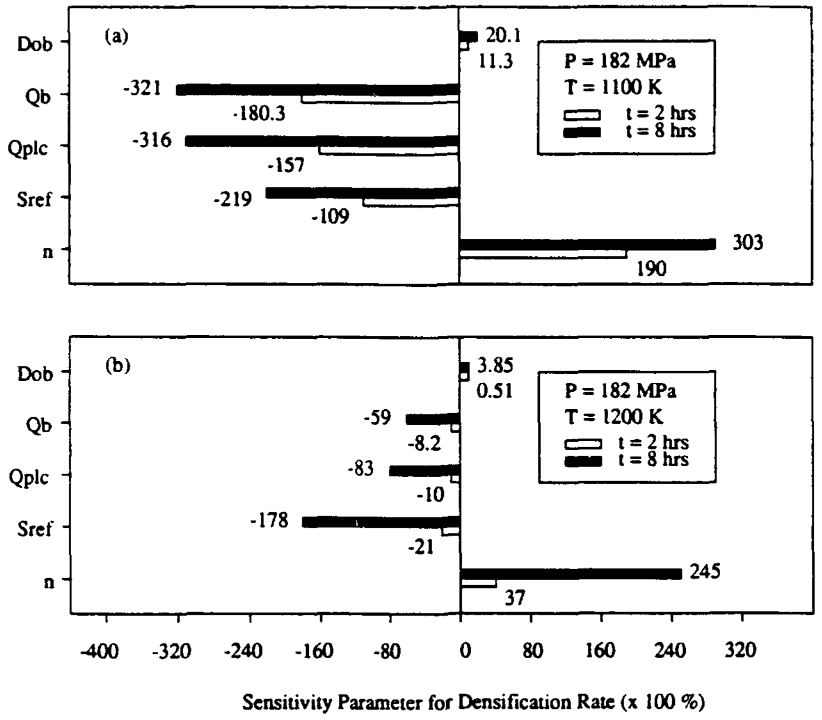

Figure 14. Sensitivity parameter for the densification rate with respect to PLC and grain boundary diffusion material properties.

determining the most critical material property parameters whose values will have to be determined with a greater degree of precision relative to the less critical parameters. Also, if we have information about the possible variation in material property data, Fig. 13 can aid us in estimating the variation in the density predictions. This is demonstrated in Fig. 15, which is a HIP diagram for TiAl, showing the relative density as a function of temperature, at a constant pressure of 182 MPa and a constant time contour of t = 1 h. Realistic variations (about their means) in material property values were used and are listed in Table 4. The cumulative errors in the predicted results are shown as error-bars in Fig. 15. The error at each point was calculated as the sum due to the assumed variation in the value of each material property. It must be pointed out that the case considered is the worst one since all the material parameters are assumed to cause either positive or

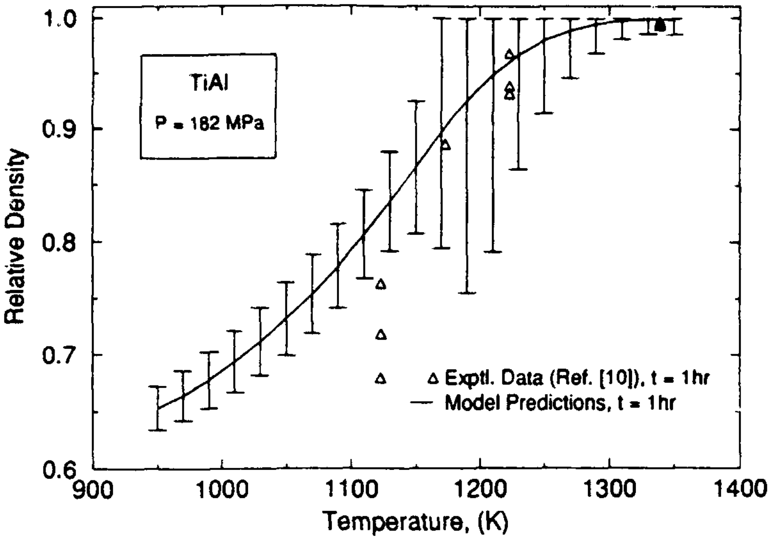

Figure 15. HIP densification diagram for TiAl ($\sigma_{ref} = 27$ MPa, $T_{ref} = 1255$°K). The error bars represent the variation in density due to uncertainty in material property.

negative deviation. Therefore, we have to determine the value of the critical material properties with a specific minimum accuracy, so as to achieve a particular accuracy in the predicted results.

Choi et al. (Ref. 16) used an extrapolation method to estimate the value of the reference stress for PLC, σ_{ref}, as 2350 MPa. This value is about four times the yield strength of TiAl at the temperature of reference ($T_m/2$) and, therefore, highly unrealistic. The good agreement between experiments and theory reported in Ref. 16 is therefore fortuitous. This reinforces the fact that material property values determined by the non-direct methods can be very misleading. It is, therefore, imperative that either direct experimental methods should be used to determine the material property values or the non-directly estimated values should be reexamined to make sure they are realistic values. In the present study creep parameters at temperatures close to the HIP temperatures were determined for bulk TiAl and were then used for comparing the experimental densification rates with the predictions of the HIP maps program. As suggested by Wadley et al. (Ref. 37), by defining the reference stress, σ_{ref}, at the strain rate, $\dot{\varepsilon}$, of 10^{-6} s^{-1} at T_{ref}, where T_{ref} is the temperature at which the creep parameters in this study were determined, we can write the creep rate equation as:

$$\dot{\varepsilon} = 10^{-6} \bullet \left(\frac{\sigma}{\sigma_{ref}}\right)^{n} \bullet \exp\left[\frac{-Q_{crp}}{R \cdot T_m}\left\{\frac{Tm}{T} - \frac{Tm}{T_{ref}}\right\}\right] \tag{17}$$

The experimentally determined strain rate dependence on stress for TiAl, at a temperature of 1255°K is shown in Fig. 16. Fitting the data to Eq. (17) gives a value of 27 MPa for σ_{ref} at a T_{ref} of 1255°K. Substituting these values instead of 2350 MPa and T_{ref} of $T_m/2$ (as in Ref. 30) the HIP map for TiAl shown in Fig. 15 was constructed. Except for the values of σ_{ref} and T_{ref}, all the other material property data used in the HIP map construction are the same as used in Ref. 16. The confidence in the HIP map program predictions is now enhanced because good agreement between model predictions and experimental data have been obtained using realistic values for the material properties.

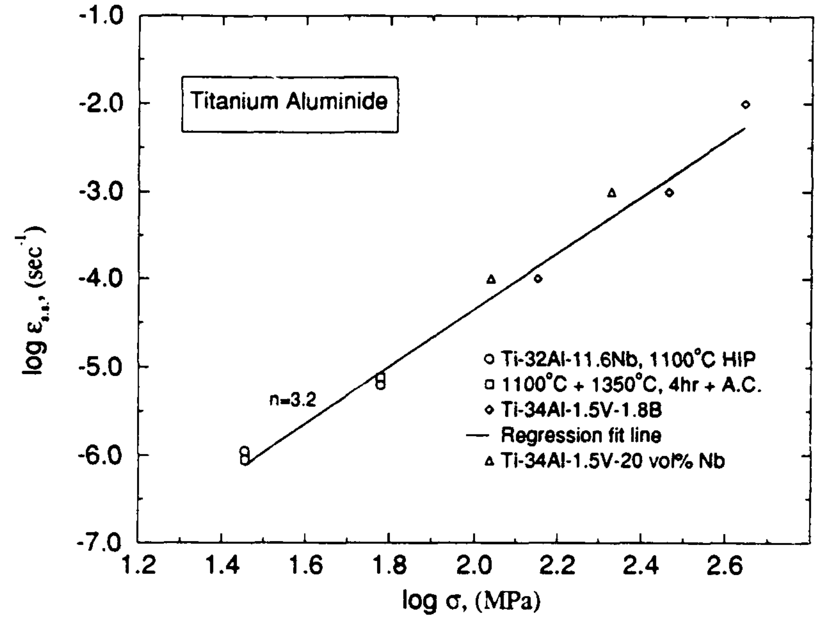

Figure 16. Steady state creep rate of TiAl at 982°C (1255°K).

Using these material property data for monolithic $MoSi_2$, the sensitivity analysis was repeated, in order to assess the sensitivity of the model predictions to the accuracy with which material property data for this material was known. The least accurately known parameter for $MoSi_2$ was judged to be the pre-exponent for volume/bulk diffusion, δD_0. This parameter was estimated, to attain the best fit between experimental data and the HIP modeling calculations. It is therefore important to understand how sensitive the calculations are to variations in δD_0. The sensitivity analysis was carried out for this parameter, as well as for the pre-exponent for grain boundary diffusion, the PLC exponent, PLC activation energy, and PLC reference stress. The results are plotted in Fig. 17. The effect of δD_0 is seen to be negligible, and the PLC exponent and reference stress have the strongest effect.

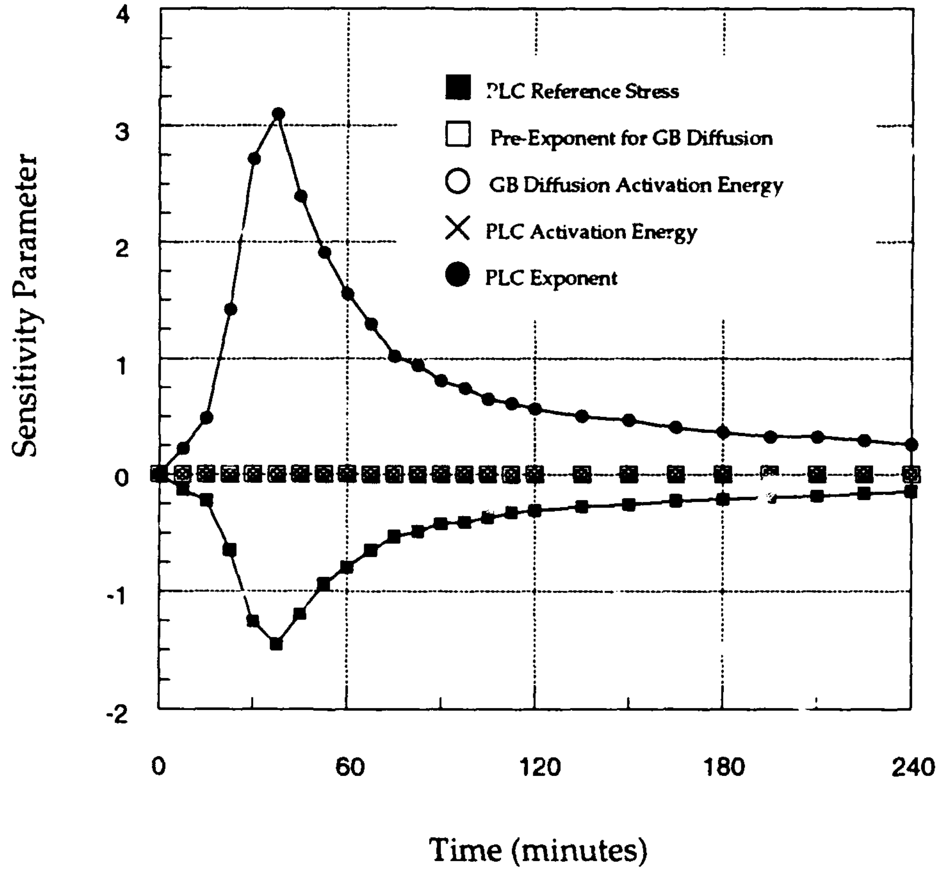

Figure 17. Sensitivity of HIP model predictions on several material property parameters for $MoSi_2$.

3.3 Reinforcement/Matrix Compatibilities

The high temperatures required to HIP consolidate $MoSi_2$-based composites introduces the possibility of reaction between the matrix and reinforcement materials. A variety of ductile reinforcements were mixed with $MoSi_2$ powder and HIPed. The details of the resulting reactions were examined by optical and electron microscopy. Ductile reinforcements examined in this program included W, Ta, Mo, and Nb. Nb reinforcements were used for the majority of this program, so the reaction between $MoSi_2$ and Nb was characterized in depth and is discussed separately in Section 3.3.2.

3.3.1 Mo, W, and Ta Reinforcements

Commercial purity Mo, W, and Ta wires were HIPed with $MoSi_2$ powder at 1700°C/4 h, and the reaction zones produced around the wires were examined metallographically. EDX was used to identify the reaction products based on chemistry. It should be noted that EDX cannot distinguish between compounds with identical chemistry but different crystal structures, e.g., the hexagonal and tetragonal forms of Mo_5Si_3. This point will be addressed for Nb reinforcements in Section 3.3.2.

Mo wire reinforcements showed the largest, but least complex reaction zone, as seen in Fig. 18. The width of the reaction layer was typically 90 µm, and was composed entirely of the Mo_5Si_3 phase. The Si content was quite uniform across the reaction zone, and the unreacted Mo wire showed a detectable (1-2 at.%) amount of dissolved Si. A 20 µm wide band of porosity was observed in the reaction zone adjacent to the $MoSi_2/Mo_5Si_3$ interface, which are Kirkendall voids resulting from the difference in diffusion coefficient for Si and Mo. These voids were observed in the W, Ta, and Nb reinforced material as well, and always were localized in a band near the interface between the $MoSi_2$ and the first reaction layer.

Figure 18. Mo wire in $MoSi_2$ HIPed at 1700°C/4 h.

W wire resulted in a more complex interface (Fig. 19). The reaction layer was thinner than the $Mo/MoSi_2$ case (~ 40 µm), indicating slower diffusion kinetics for the Mo-Si-W system. Two distinct layers were visible in the reaction zone. The outermost layer was composed of $(Mo,W)_5Si_3$. The Mo:W ratio changed from about 5:1 near the $MoSi_2/(Mo,W)_5Si_3$ interface, to 1:5 near the inner reaction layer. This outer reaction layer was commonly observed to be heavily microcracked in the $W/MoSi_2$ composites. Inside this layer was a less sharply delineated layer, with some elongated grains reaching into the $(Mo,W)_5Si_3$ layer. The inner reaction layer was composed of W_5Si_3, with only trace amounts of Mo present. Si was not detected in the W wire, a result of the low Si solubility in W, which even at the HIP temperature of 1700°C is only ~ 1.5 at.%. Occasional grains of composition W_3Si were found, but these did not form a continuous band around the W wire.

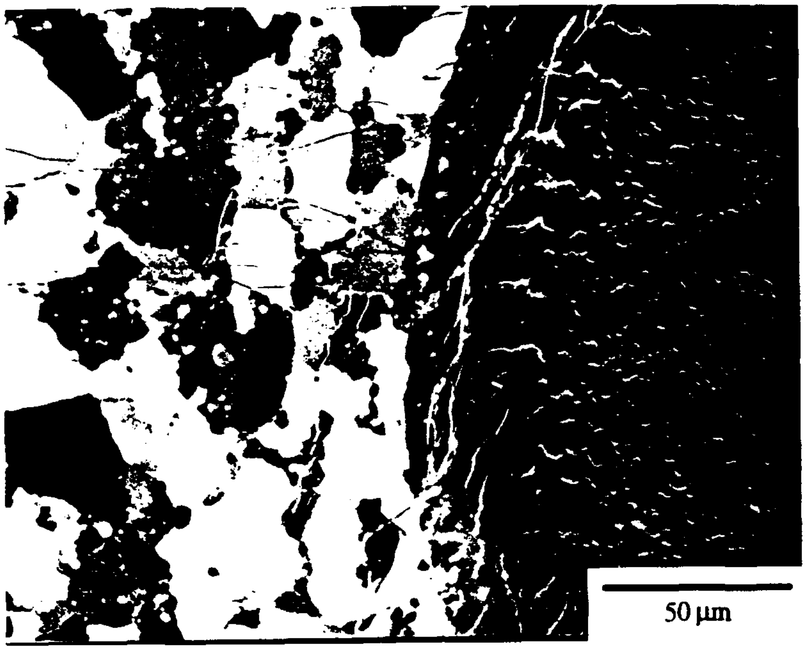

Figure 19. W wire in $MoSi_2$ HIPed at 1700°C/4 h.

Ta wire reacted with $MoSi_2$ in a fashion very similar to W. The reaction zone had two distinct layers, and was about 30 µm thick (Fig. 20). The outer reaction layer was composed of $(Mo,Ta)_5Si_3$, with the Mo:Ta ratio varying from 4:1 near the outer interface to 1:4 near the inner edge. Adjacent to this ternary layer was a layer of Ta_5Si_3 with

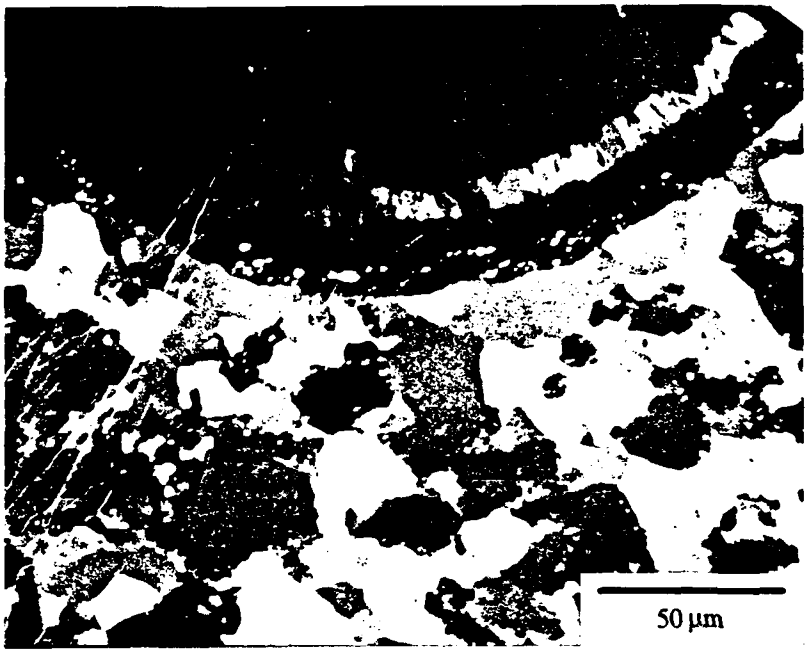

Figure 20. Ta wire in $MoSi_2$ HIPed at 1700°C/4 h.

negligible Mo content. As in the $MoSi_2$/W specimen, extensive microcracking was observed in the reaction layer. Kirkendall voids were present, and appear as bright spots in the outer reaction layer in Fig. 20.

3.3.2 Nb Reinforcements: Reaction Zone Details

Nb reinforcements were used for the majority of this program, so a more detailed analysis of the $MoSi_2$/Nb reaction zone was undertaken. Both EDX and electron diffraction were used to identify the reaction products.

The structure of the reaction zone around a Nb particle in $MoSi_2$ + Nb HIPed at 1700°C/4 h is shown in Fig. 21. Two layers can clearly be seen, although three layers are actually present. The outermost layer shows the usual Kirkendall porosity, and is composed of $(Mo,Nb)_5Si_3$. Electron diffraction showed that this layer had the tetragonal $D8_m$ structure common to many transition metal 5-3 silicides. The Mo:Nb ratio varied

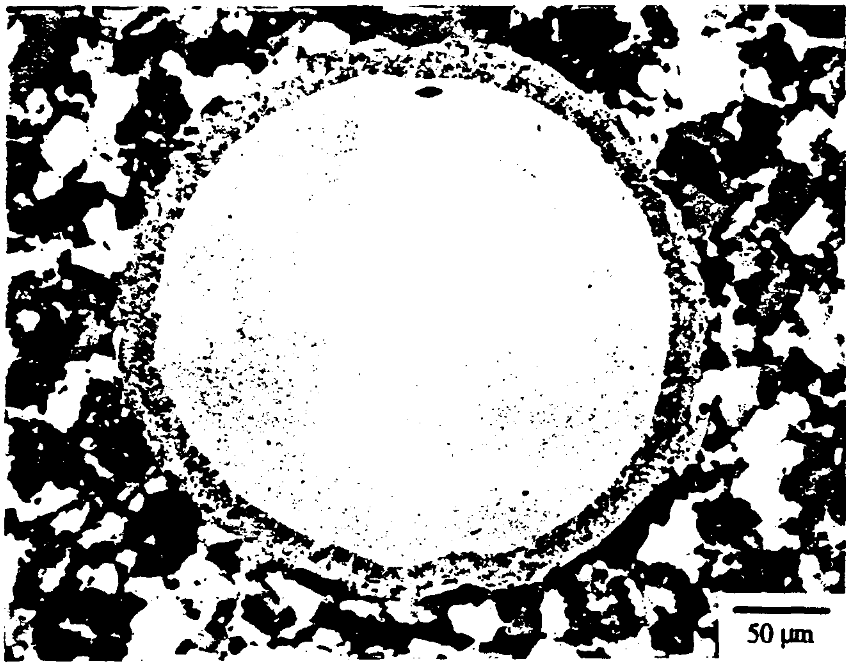

Figure 21. Nb powder particle in $MoSi_2$ HIPed at 1700°C/4 h.

from about 2:1 to 1:5 across this layer, going down with increasing distance from the $MoSi_2/(Mo,Nb)_5S_3$ interface. Adjacent to the outer layer was a layer of Nb_5Si_3 with very low Mo content (< 3 at.%). The crystal structure of this layer was also $D8_m$. The innermost layer was Nb_5Si_3 with the hexagonal $D8_8$ structure. C and O are common impurities in Nb, and it is likely that these impurities diffuse out of the Nb particles into the Nb_5Si_3 layer during HIPing and stabilize the $D8_8$ structure. The $D8_8$ structure is stabilized by interstitial impurities in a variety of $D8_m$ 5-3 silicides, including Nb, Mo, V, Cr, Ta, and W silicides. The Nb-$MoSi_2$ reaction produces a reaction product with a refined grain size. The grain diameter normally observed in the $MoSi_2$ matrix is 5-50 µm (see Figs. 18-21). However, within the reaction zone the grain diameters are typically 1-5 µm, with some grains 250 nm or less. This grain refinement through reaction effect was explored in more detail using $MoSi_2$ + Ti HIP reacted composites, and is discussed in Section 3.5.

Isolated grains with approximately a 2:1 Nb to Si ratio were observed in the Nb/Nb_5Si_3 interface (Fig. 22). Electron diffraction showed that this phase had a tetragonal structure, with $a_o \approx 0.77$ nm and $c_o \approx 0.95$ nm. Two tetragonal Nb_3Si phases have been reported in the literature (Ref. 38), one with $a_o = 1.022$ nm, $c_o = 0.519$ nm,

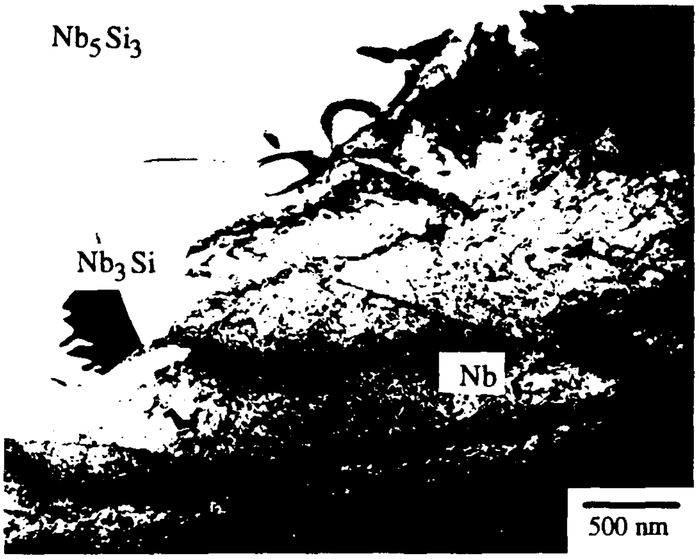

Figure 22. Nb_3Si grain in Nb_5Si_3/Nb interface.

and the second with $a_0 = 0.659$ nm, $c_0 = 1.265$ nm. The observed phase may be an off-stoichiometric form of one of these reported phases. This tetragonal phase was present only in very small quantities, and the grain size was small ~ 0.5-1.0 µm, so it is not likely that this phase plays a significant role in the properties of $MoSi_2$ + Nb composites.

The temperature dependence of $MoSi_2$/Nb reaction zone growth was determined quantitatively by HIPing $MoSi_2$ and Nb powders and measuring the reaction zone thickness as a function of temperature. The reaction zone was divided into two layers, an outer layer adjacent to the $MoSi_2$ matrix composed of Mo-rich $(Mo,Nb)_5Si_3$ and an inner layer composed of Nb-rich $(Nb,Mo)_5Si_3$. The narrow and discontinuous Nb_3Si layer was neglected in this analysis. The reaction layer thicknesses are tabulated in Table 5.

Table 5. Measured Reaction Layer Thickness After HIPing $MoSi_2$ + Nb for 1 Hour at 207 MPa, as a Function of Temperature

Temperature (°C)	Inner Reaction Layer Thickness (µm)	Outer Reaction Layer Thickness (µm)
1200	2.24	1.56
1300	5.67	3.82
1400	9.20	5.73

The growth coefficient ($k = x / \sqrt{t}$, x = reaction layer thickness, t = reaction time) of the reaction zone around the fine Nb powders was from ~ 2-5 times slower than reaction rates which have been measured by other studies (Refs. 39,40). This slower rate is due to the presence of a high impurity level in the fine Nb powder. Impurities in the reaction zone, such as O and C, will slow the rate of Si diffusion significantly. In addition, impurities stabilize the $D8_8$ hexagonal structure, which has a five times slower Si diffusion rate than the $D8_m$ tetragonal structure associated with pure $(Mo,Nb)_5Si_3$ (Ref. 39). While the Nb particles contain a high enough impurity level to cause the inner Nb-rich reaction layer to form with the $D8_8$ structure, the impurities do not diffuse to the outer Mo-rich layer in concentrations high enough to cause this outer layer to also form with the $D8_8$ structure. As a result, the outer layer forms with the pure $D8_m$ structure.

The Arrhenius plot of log growth constant as a function of inverse absolute temperature is shown in Fig. 23, for the coarse Nb powder. The data from Ref. 39 is also plotted in Fig. 23, as a pair of continuous lines. The data for the inner, Nb-rich reaction layer agrees well with the Ref. 39 data. The data for the outer reaction layer shows a significantly higher growth constant over the low end of the temperature range than that measured in Ref. 39. It is not clear what gives rise to this discrepancy, but it should be noted that the outer reaction layer is typically filled with Kirkendall voids which can make it difficult to accurately measure the layer thickness.

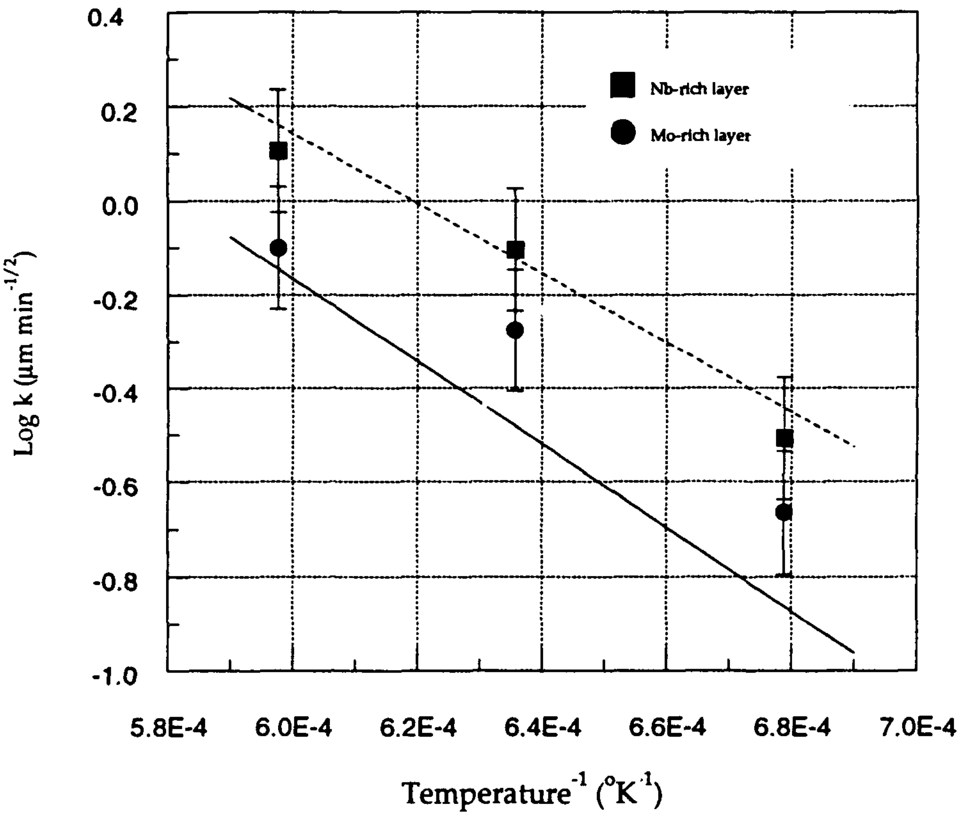

Figure 23. Log k vs. inverse absolute temperature for the Mo-rich and Nb-rich reaction layers. The data from Ref. 39 is plotted as a dotted line (Nb-rich layer) and a solid line (Mo-rich layer).

The inner reaction layer grows at a faster rate than the outer layer over the entire temperature range, as can be seen in the graph in Fig. 24. In this graph, the reaction zone thickness after one hour exposure is plotted as a function of temperature. In addition, the inner reaction layer appears to be more sensitive to temperature, i.e., the growth rate of the inner reaction layer increases more than the outer reaction layer for a given increase in temperature.

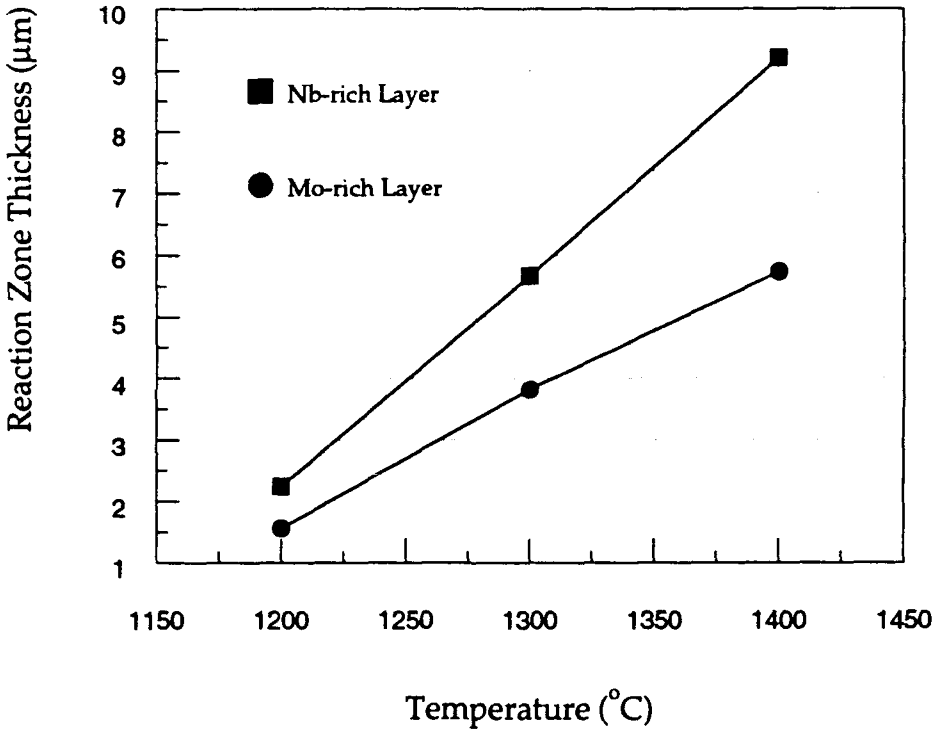

Figure 24. Reaction zone thickness after 1 h as a function of temperature.

3.4 Ductile Phase Reinforcement Toughening

3.4.1 Background

The possibility of toughening brittle materials through the addition of ductile reinforcements was demonstrated about 20 years ago (Refs. 41-43). In this program the plausibility of toughening $MoSi_2$ through the addition of Nb reinforcements was explored, and the effect of reinforcement morphology on toughness was examined in detail.

The increase in toughness of a material due to the presence of ductile reinforcements is largely due to the crack energy dissipation caused by ductile reinforcements bridging the cracks (Refs. 44,45; Ref. 46 is a good source for historical background). As the crack opening displacement (COD) increases under the applied load, the reinforcements stretch, dissipating energy and shielding the crack from the full applied load. The increase in toughness due to crack bridging can be written (Ref. 44):

$$\Delta G_c = V_f \int_0^{u^*} \sigma(u)du \tag{18}$$

where $\sigma(u)$ is the stress supported by the reinforcements as a function of the COD, u. The integration limit u^* is simply the maximum COD attained before the reinforcement fails. V_f is the reinforcement area fraction in the plane of the crack. The formulation can be written in terms of the more familiar critical stress intensity factor using this relationship:

$$G_c = \frac{K_{1c}^2}{E}(1-\nu^2) \tag{19}$$

where E is the Young's modulus and ν is Poisson's ratio. Assuming $\nu \approx 1/3$, an increase in toughness from G_c to $G_c + \Delta G_c$ produces an increased stress intensity factor of:

$$K_{1c} = \left[\left(K_{1c}^{o}\right)^2 + \frac{9E\Delta G_c}{8}\right]^{1/2} \tag{20}$$

where K_{1c}^{o} is the original, non-toughened critical stress intensity factor and ΔG_c is given by Eq. (18).

A failure of this approach to formulating the toughness increase is that it does not adequately account for reinforcement morphology. For example, a dispersion of Nb powder reinforcements could have the same V_f as an array of continuous Nb wires, yet the results of this study show clearly that Nb wires are more potent tougheners of $MoSi_2$ than Nb powder. The limitation of the formulation is due to the fact that for discontinuous reinforcements, the propagating crack is able to deflect around the reinforcements by traveling through the weak, brittle matrix/reinforcement interface. A crack propagating in this way experiences no bridging, although a modest toughness increase should be seen due to crack deflection effects. Toughness increase due to crack deflection is thought to have this form (Ref. 47):

$$K_{1c} = \frac{K_{1c}^{o}}{\cos^2\left(\theta/2\right)} \qquad (21)$$

where θ is the crack deflection angle and K_{1c}^{o} is the fracture toughness with no crack deflection. Therefore, a crack deflection of 60°, which is larger than typically observed in discontinuously reinforced $MoSi_2$, will increase the toughness by only ~ 33%. Continuous reinforcements, for example wires of lamellae, cannot be avoided by cracks propagating in the direction perpendicular to the reinforcements. Therefore, the cracks in continuously reinforced composites are ensured to be bridged, regardless of V_f. Crack bridging is a more potent toughening mechanism than crack deflection, so the toughness of continuously reinforced composites will be greater than discontinuously reinforced composites if the matrix/reinforcement interface is brittle and weak.

3.4.2 Reinforcement Morphologies

Four different reinforcement morphologies were used to make $MoSi_2$ + Nb composites for this study. These included 100-200 µm diam powder (nominally -80 + 200 mesh), 250 µm diam wire, 750 µm diam wire, and 200 µm thick foil. The Nb powder was 99.8% pure, and the wire and foil were commercial grade Nb. The composites were fabricated with the goal of achieving 20 vol% reinforcing phase, but due to the vagaries of mixing powders and making fiber and foil lay-ups by hand, the volume fraction of reinforcing phase varied significantly from this goal. The powder reinforced material was typically close to 20 vol%, while the wire reinforced material varied from 15-20 vol% and the foil reinforced material varied from 25-30 vol%. The reinforcement morphology and orientation are shown schematically in Fig. 25, with the orientation of the toughness test notch indicated. After HIPing, the reinforcements quite uniformly had a ~ 15 μm thick reaction layer in the matrix/reinforcement interface. Micrographs of each reinforcement morphology are shown in Fig. 26a-d in the as-HIPed condition.

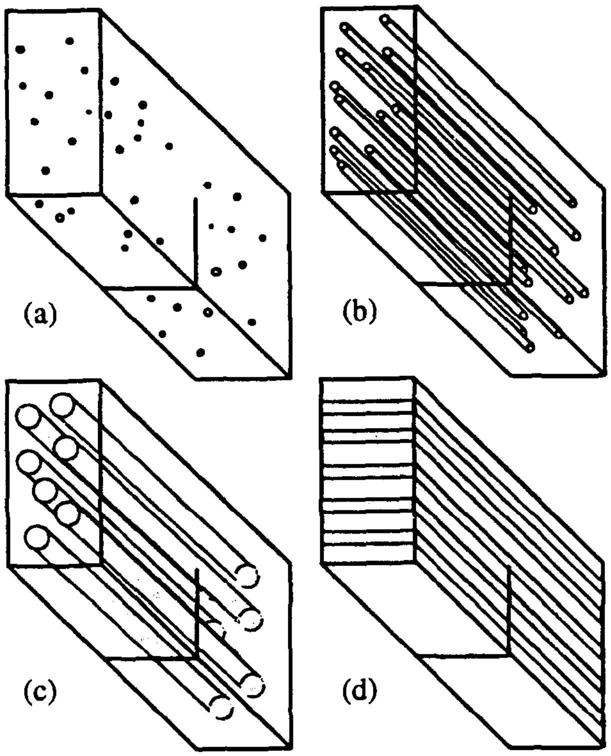

Figure 25. Reinforcement morphologies and orientations shown schematically. Orientation of notch for toughness measurements is indicated.

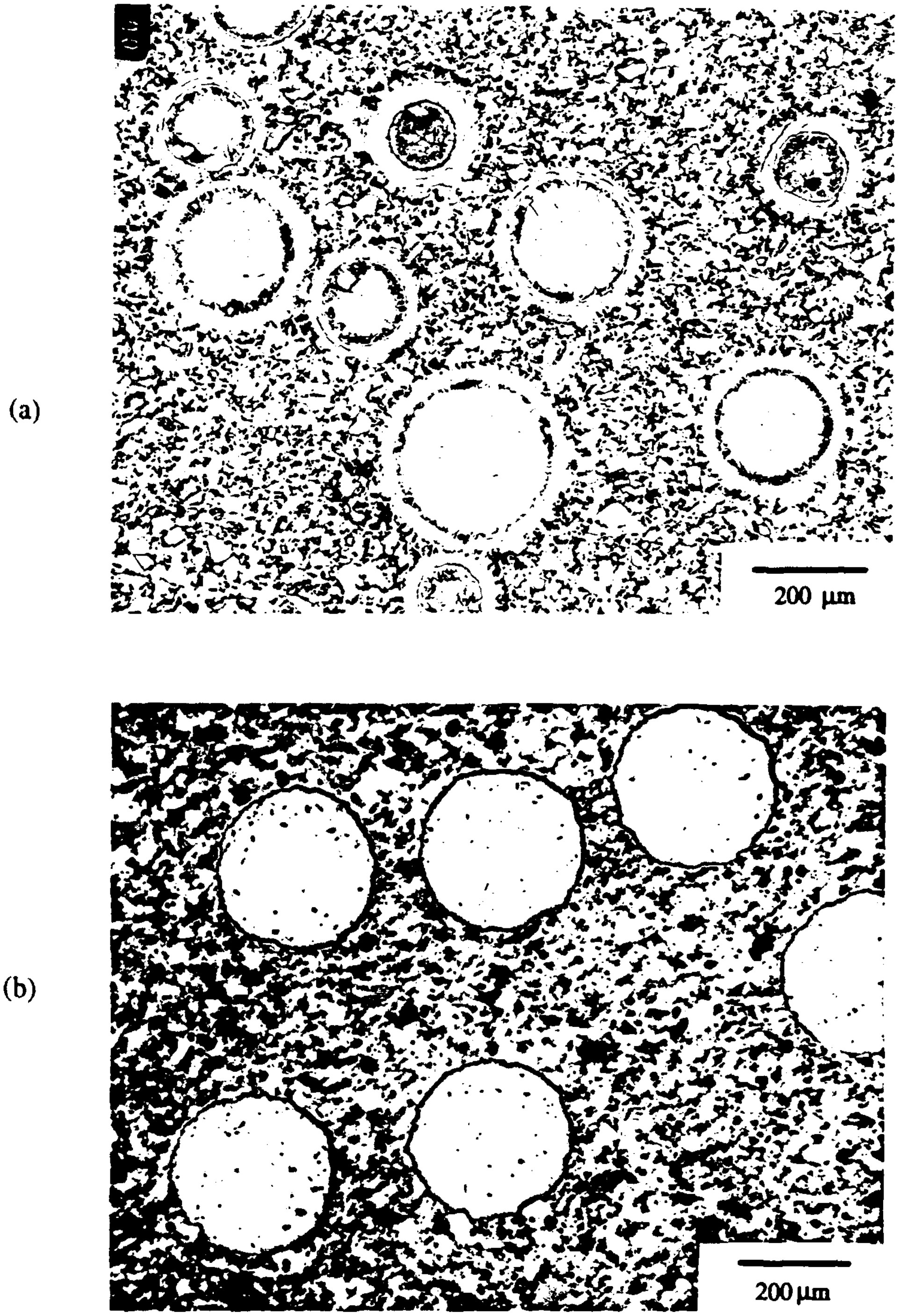

Figure 26. As-HIPed microstructure of (a) Nb powder reinforced, (b) 250 μm Nb wire reinforced, (c) 750 μm Nb wire reinforced, and (d) 200 μm Nb foil reinforced $MoSi_2$.

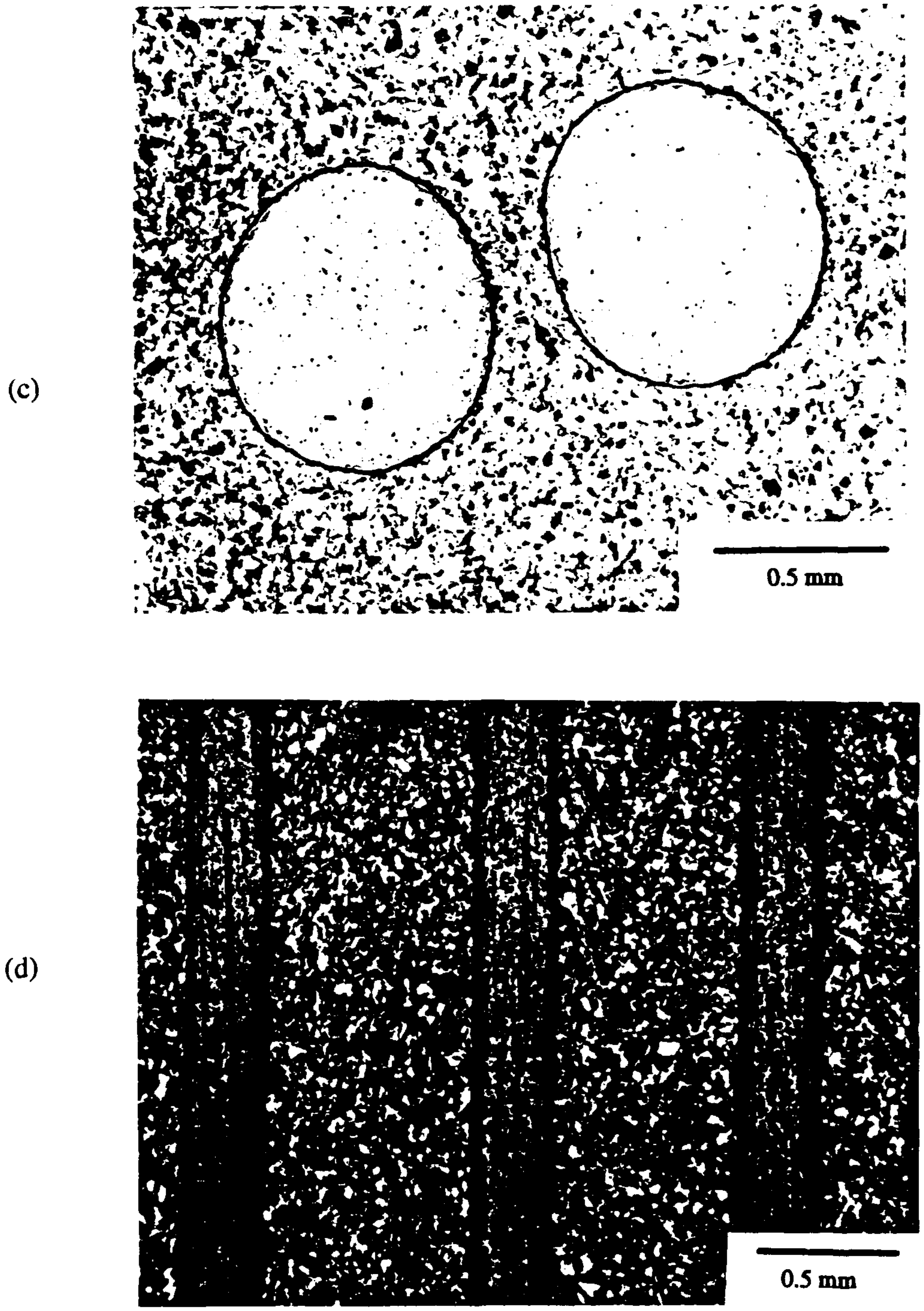

Figure 26. (continued)

3.4.3 Mechanical Property Data

The bend strength of monolithic and reinforced $MoSi_2$ was measured at temperatures between room temperature and 1400°C. High temperature testing was performed in a vacuum of ~ 10^{-6} Torr, and 4-point bending was used. The tests were performed in load control mode, and the resulting strain rate was ~ 10^{-5} s^{-1}. The specimen geometry with typical dimensions is shown in Fig. 27(a). The fracture toughness of monolithic and reinforced $MoSi_2$ was determined at room temperature using standard ASTM E399 3-point bend specimens [Fig. 27(b)].

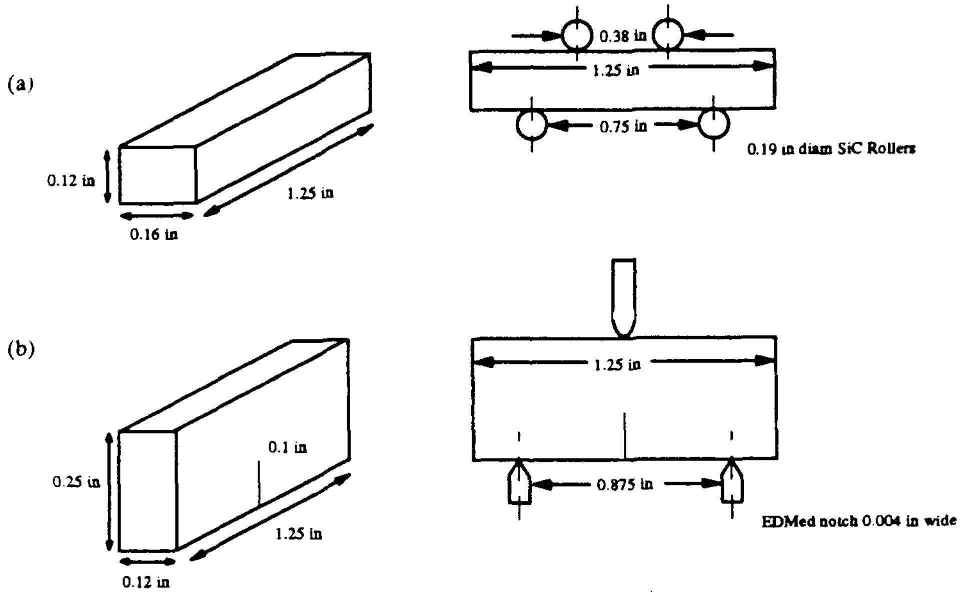

Figure 27. Typical specimen dimensions used in this program for (a) four-point bend testing and (b) three-point fracture toughness testing.

3.4.3.1 Bend Test Results

The results of the bend tests are tabulated in Table 6, and shown graphically in Fig. 28. The values in Table 6 are averages wherever multiple tests could be run, with the standard deviations included. The graph in Fig. 28 includes all the data points, to give an idea of the scatter in the data.

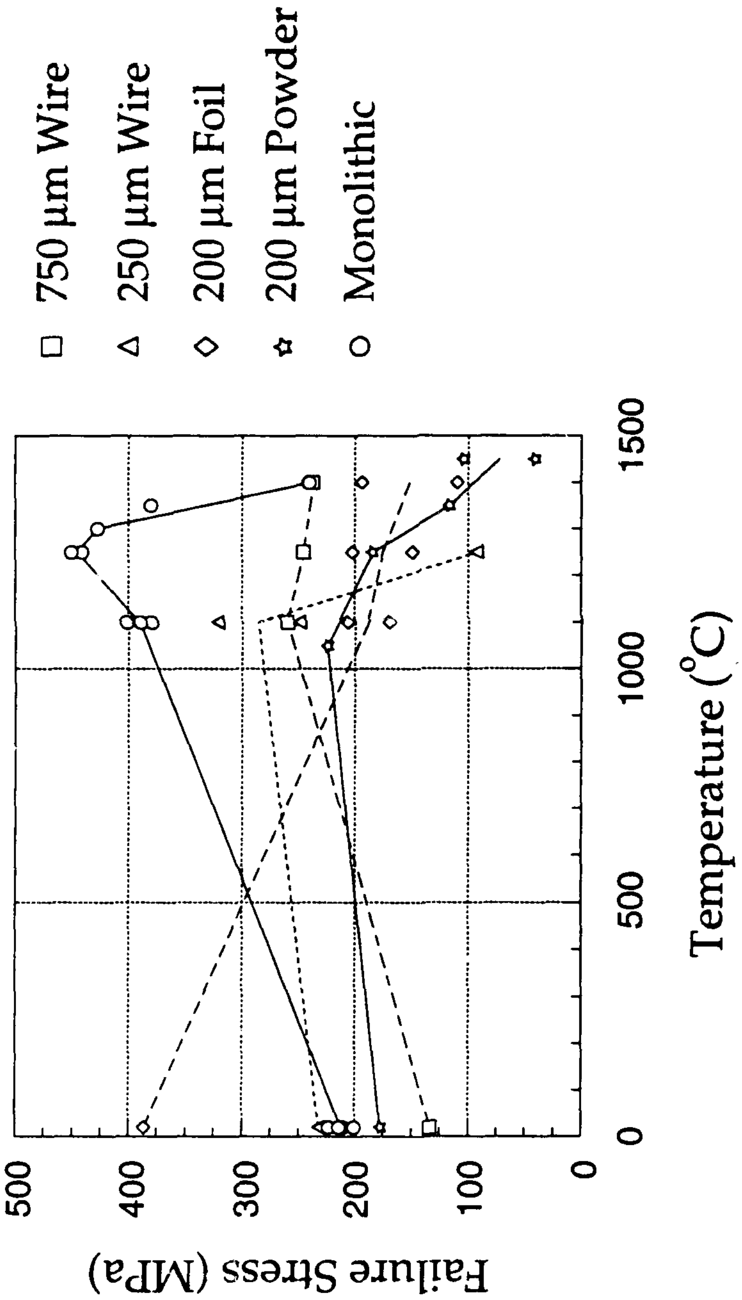

Figure 28. Ultimate four-point bend strengths of monolithic and reinforced MoSi2 as a function of temperature.

Table 6. Ultimate Four-Point Bend Strengths (MPa) of Monolithic and Reinforced $MoSi_2$

Specimen	20°C	1050°C	1100°C	1250°C	1300°C	1350°C	1400°C	1450°C
Monolithic	212±8	-	390±11	446±6	427	-	241±1	-
200 μm Nb powder	177	224	-	184	-	117	-	72±44
250 μm Nb wire	232	-	286±51	92	-	-	-	-
750 μm Nb wire	133	-	260	245	-	-	237	-
200 μm Nb foil	386	-	188±26	176±38	-	-	152±60	-

The rising ultimate bend strength as a function of temperature of monolithic $MoSi_2$ reflects the very low fracture toughness of $MoSi_2$ at low temperatures, rather than any intrinsic strengthening mechanisms (as observed in many intermetallics with the $L1_2$ structure, for example). The extreme flaw-sensitivity of the material, coupled with the presence of a high flaw density in even the highest quality HIPed $MoSi_2$, causes the specimens to fail long before the true ultimate strength is reached. As expected in material with these characteristics, no yielding is detected and failure takes place at a low stress level before any macroscopic plasticity is observed. The same type of behavior is seen, to a lesser degree, in the reinforced material. The foil reinforced specimens are an exception that will be discussed later. The wire and powder reinforced composites are weak at room temperature, despite the fact that they have higher toughness than monolithic $MoSi_2$, as will be seen in Section 3.4.3.2. This is due to the fact that these materials naturally contain an even higher flaw density than monolithic $MoSi_2$, which is a result of the brittle, Kirkendall void containing reaction layer surrounding the Nb reinforcements, as well as thermal expansion mismatch between matrix and reinforcement, to a lesser degree. The increased K_{1c} of these composites is offset by the large number of critical flaws in the matrix, and the composites fail well before reaching the true ultimate bend strength.

The lamellar composites, reinforced with 4-5 layers of 200 μm thick Nb foil, are much stronger than the other specimens at room temperature. The lamellar composites have a high enough fracture toughness to prevent premature failure of the specimens. In addition, the Nb layers themselves are strong at room temperature (the room temperature tensile strength of Nb is 400-500 MPa), and contribute to the bend strength of the composite.

At elevated temperatures, the toughness of the $MoSi_2$ matrix is no longer a factor limiting bend strength. Instead, the Nb reinforcements limit strength due to the relative weakness of Nb at elevated temperature (the tensile strength of Nb is 100-200 MPa at 1100°C). The bend strength at elevated temperatures is actually below that expected from a simple rule of mixtures approach, based on the relative volume fractions of matrix and reinforcement.

3.4.3.2 Fracture Toughness Test Results

Fracture toughness of monolithic, Nb powder-, Nb wire-, and Nb foil-reinforced $MoSi_2$ composites was determined by measuring K_{1c} values according to ASTM E399 guidelines. The test specimen geometry is shown in Fig. 27(b). All tests were performed at room temperature. In the early stages of this study, specimens were precracked in far-field compression prior to testing. However, no differences in K_{1c} were observed when precracked and non-precracked specimens were compared, so the time consuming precracking procedure was eliminated from the majority of this study. In addition, specimens frequently failed during the precracking procedure, wasting valuable specimens. The insensitivity of $MoSi_2$ to precracking is due to the high flaw density that naturally occurs in HIPed $MoSi_2$ powder, in the form of porosity and fine impurity particles. These flaws serve quite adequately as precracks to initiate the cracking process, and additional cracks introduced by compression precracking are superfluous.

The average K_{1c} values measured for each reinforcement morphology are listed in Table 7 along with standard deviations. The data is also shown graphically in Fig. 29. The reinforced $MoSi_2$ can be seen to be significantly tougher than the monolithic material. In addition, the reinforcement morphology clearly has a significant effect on the composite toughness.

Table 7. Average K_{Ic} Values for Monolithic and Reinforced $MoSi_2$, With Standard Deviations

Specimen Type	K_{Ic} $(MPa\sqrt{m})$
Monolithic	3.6 ± 0.6
200 µm Nb powder reinforced	5.7 ± 0.5
250 µm Nb wire reinforced	9.1 ± 0.9
750 µm Nb wire reinforced	11.3 ± 4.1
200 µm Nb foil reinforced	18.0 ± 2.0

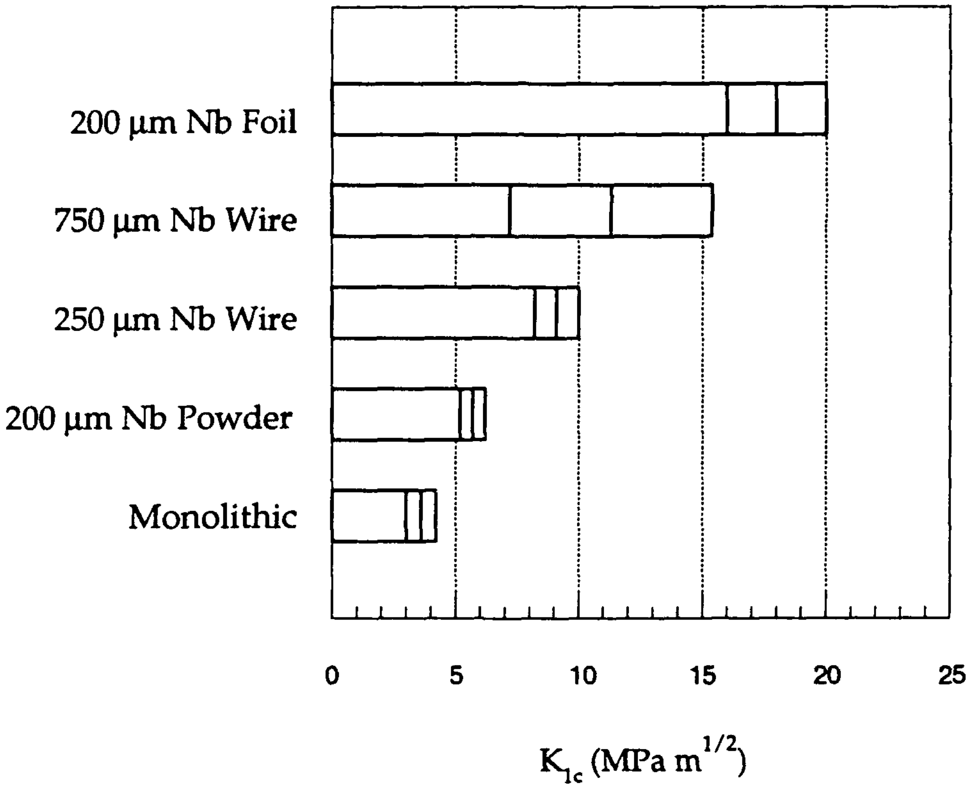

Figure 29. K_{Ic} values for monolithic $MoSi_2$ and Nb powder-, Nb wire-, and Nb foil-reinforced $MoSi_2$. Each bar shows the lowest, average, and highest recorded value.

The Nb powder produces the smallest toughness increase, largely because the crack is able to propagate around the spherical reinforcements, preventing them from bridging the crack. This can be seen in Fig. 30, a typical fracture surface in Nb powder reinforced composites. There is no evidence of plasticity in any of the exposed particles in the fracture surface, and the crack in almost every case traveled through the matrix/reinforcement interface, rather than the reinforcement.

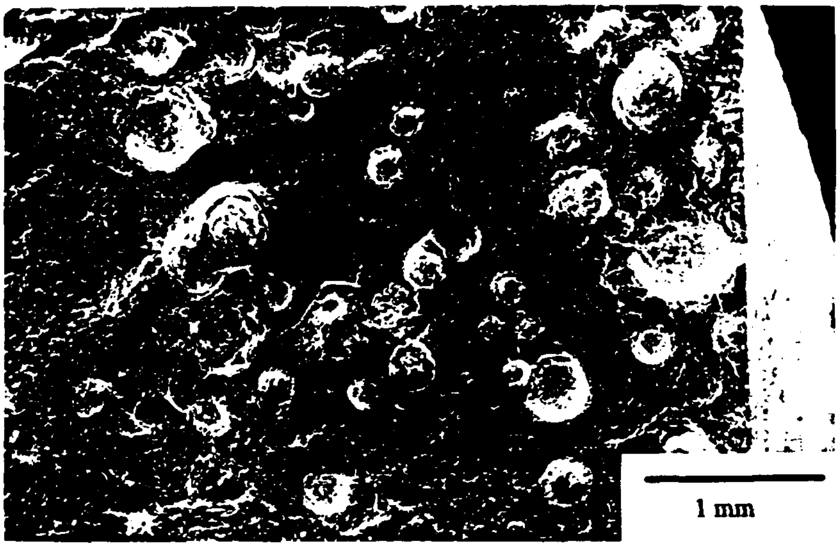

Figure 30. Fracture surface in $MoSi_2$ + 20 vol% 200 µm diam Nb powder reinforced specimen.

The 250 µm diam wire reinforced material was next in the hierarchy of increasing fracture toughness improvement. Figure 31 shows a typical fracture surface. The crack is clearly bridged by the Nb wires, most of which show substantial plastic deformation. Several of the wires failed in a brittle fashion, as evidenced by their flat, cleaved fracture surfaces. It is not clear why some wires failed brittly, whereas others exhibited extensive plasticity, but this mixed behavior was commonly observed in the 250 µm wire reinforced specimens. A plausible explanation is that the wires are strain rate sensitive, and the <u>local</u> crack velocity (which can vary enormously) determines the nature of the wire fracture.

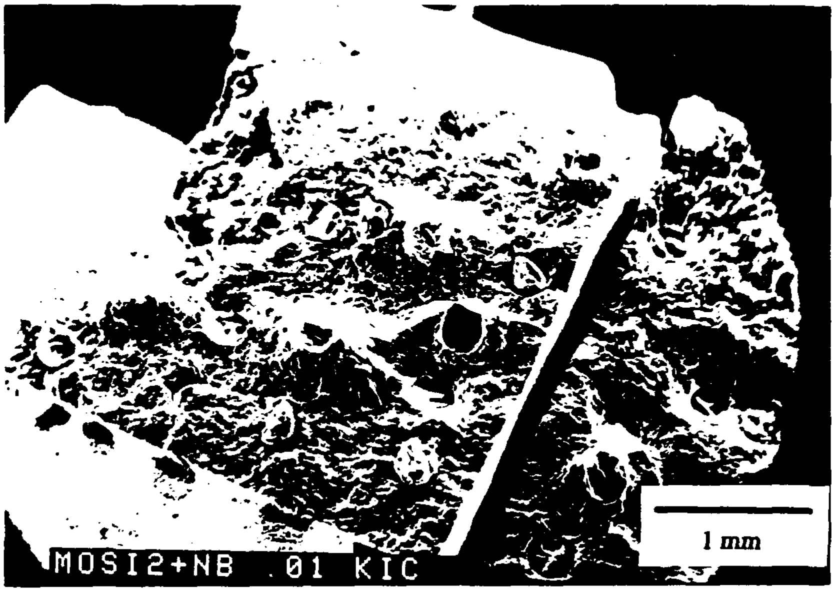

Figure 31. Fracture surface in $MoSi_2$ + 15 vol% 240 μm diam Nb wire reinforced specimen.

The 750 μm diam wire reinforced material displayed slightly higher toughness on average than the composites with 250 μm diam wire. Figure 32 shows a typical fracture surface in material reinforced with the heavier wire. All of the Nb wire reinforcements in these specimens failed in a brittle fashion. A closer view of a fractured wire is seen in

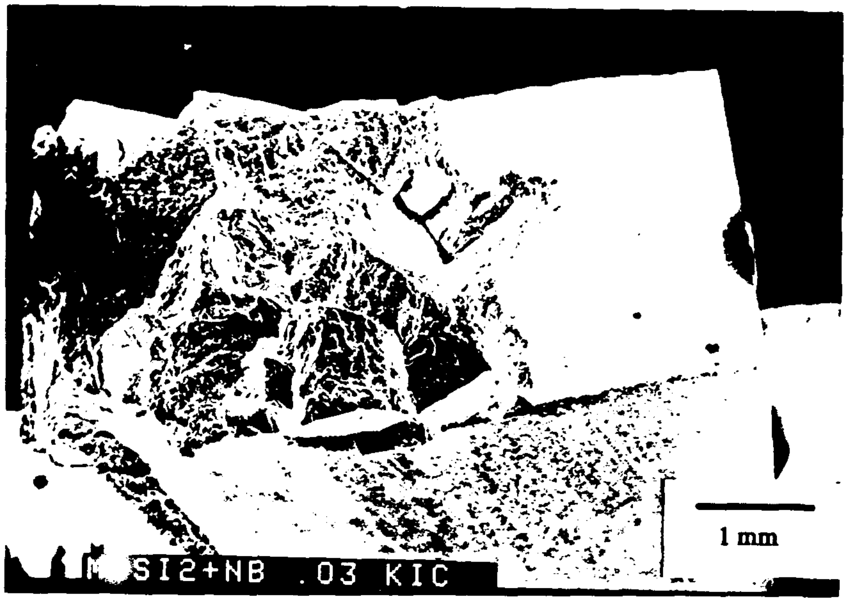

Figure 32. Fracture surface in $MoSi_2$ + 20 vol% 750 μm diam Nb wire reinforced specimen.

Fig. 33, where the cleavage facets are clearly visible. Cleavage fracture cannot absorb as much of the crack energy as ductile fracture, but it must be remembered that the diameter of the thicker wires is 3x that of the fine wires, which results in a 9x larger cross sectional area for the thick wires. The cleaved, thick wires may absorb more energy than the ductile thinner wires despite the plasticity of the latter, because the energy absorbed is directly related to the cross sectional area (Ref. 44).

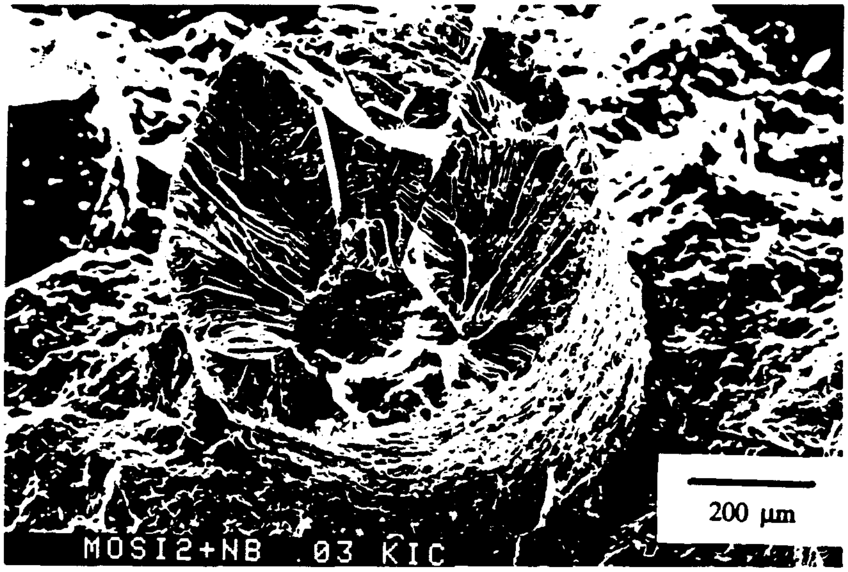

Figure 33. Fracture surface of 750 μm wire, showing brittle cleavage fraction. Note extensive matrix/reinforcement decohesion.

The 200 μm Nb foil reinforced composite showed the largest increase in toughness, roughly 5 times higher than the unreinforced material. The fracture surface (Fig. 34) is extremely non-planar, and the foil reinforcements clearly bridge the cracks. A closer view of a crack-bridging reinforcement is shown in Fig. 35. The Nb foil is highly plastically deformed, as can be seen by the extreme distortion of the initially straight, parallel scratches in the surface of the reinforcement in Fig. 35. In addition to crack bridging, two other toughening mechanisms are apparently operating. The first is crack multiplication, which dissipates crack energy by creating large amounts of new crack surface at a subcritical stress level. Several major cracks have evidently passed

Figure 34. Fracture surface of 200 µm thick foil reinforced $MoSi_2$. The smooth segment on the right is one surface of the stress concentrating notch in the K_{1c} specimen.

Figure 35. Crack bridging Nb foil reinforcement viewed edge-on, showing extensive plasticity.

through the specimen in Fig. 34 simultaneously, resulting in a complex fracture surface with numerous cracks outside of the principal crack plane. The second toughening mechanism results from the extensive debonding visible along the matrix/foil interface.

The reaction layer in this interface is weak, and fails as the foil reinforcement deforms plastically. Failure along the interface increases the decohesion length, i.e., the distance along which the reinforcement is unconstrained by the matrix and can freely deform. This in turn increases the dissipation of the crack energy, as shown in Ref. 44.

3.4.4 Discussion and Comparison to Theory

The test results in Section 3.4.3.2 clearly show that $MoSi_2$ can be toughened by Nb reinforcements, but questions arise when the observed toughness increases are compared quantitatively to theoretical calculations. Using the formalism developed in Ref. 44 for the increase in toughness, ΔG_C, due to ductile tougheners, the composite critical stress intensity factor can be written in this form (see Section 3.4.1):

$$K_{1c} = \left[\left(K_{1c}^{o}\right)^{2} + \frac{9E}{8} C V_f \sigma_o a_o\right]^{1/2} \qquad (22)$$

where K_{1c}^{o} is the monolithic critical stress intensity, E is the reinforcement Young's modulus, V_f is the reinforcement area fraction in the crack plane, σ_o is the reinforcement yield stress, and a_o is <u>half</u> the reinforcement thickness in the crack direction. The constant C relates to the decohesion length of the reinforcements. It is low for reinforcements strongly bonded to the matrix, and high for weakly bonded reinforcements that easily break away from the matrix. In Ref. 44, C was found to be between 1.6 and 6. Reference 45 reviewed a wider range of the literature and found values between 0.5 and 8. Using <u>conservative</u> values for all parameters,

K_{1c}^{o} = 4.6 MPa $\sqrt{m}$
E = 103 GPa
C = 4 (estimated)
V_f = 0.15
σ_o = 300 MPa
a_o = 100 µm,

the expected critical stress intensity factor is calculated as $K_{Ic} = 45.9$ MPa$\sqrt{m}$, more than twice the highest value measured.

In the case of the 750 μm diam wire reinforcements, it is clear that the wires fail before yielding, so it is inappropriate to use the yield stress of Nb for σ_o. Using the measured value of K_{Ic} (Table 7) for the thick wire reinforcements, 11.3 MPa$\sqrt{m}$, a reverse calculation can be performed to solve for σ_o in Eq. (22). The geometric parameters measured for the 750 μm diam wire composites were:

$V_f = 0.22$

$a_o = 375$ μm,

which leads to a value of $\sigma_o = 2.8$ MPa (all other parameters in the calculation were the same as those given in the previous paragraph). The parameter C is not well known and leads to uncertainty in the value of σ_o, but it should be noted that it probably does not vary by more than a factor of 3, which will result in an inversely proportional variation in the value of σ_o at a given K_{Ic} value. Despite the fact that the thick wires are apparently brittle (see Figs. 32,33), it is doubtful that they fail at a stress level anywhere near 2.8 MPa. A similar calculation for the Nb foil reinforced composite using these values:

$K_{Ic} = 18.0$ MPa$\sqrt{m}$

$V_f = 0.29$

$a_o = 110$ μm

generates a value of $\sigma_o = 20.5$ MPa. This stress value is slightly more credible, except that in the foil reinforced composites, the reinforcements obviously deformed plastically (Fig. 35) which occurs at a stress of at least 300 MPa.

It is clear that the widely used theoretical formulation developed in Ref. 44 significantly overestimates the actual toughness increases accrued by reinforcing $MoSi_2$ with Nb. The quantitative discrepancies between theory and experiment may be partially a result of the high flaw density found in HIPed $MoSi_2$ powder, which cause the matrix to fail at artificially low loads, leading to an apparently low value of K_{Ic}. In addition, the Nb reinforcements can be brittle (e.g., the 750 µm wire reinforcements), and may be susceptible to strain rate effects (e.g., the 250 µm wire discussed in Section 3.4.3.2), which lead to ambiguities in the calculations.

A more fundamental problem with the theoretical formulation is the insensitivity to reinforcement morphology. The best illustration of the problem is seen by comparing the theoretically expected toughness increases for the 250 µm diam wire reinforced composites and the 200 µm thick foil reinforced composites. As far as Eq. (22) is concerned, the only differences between these reinforcements are in the V_f and a_o terms. Using the values listed at the beginning of this section and the following measured values:

	Wire	Foil
V_f	0.16	0.28
a_o	125 µm	105 µm

The expected values for K_{Ic} are:

$$K_{Ic}\text{ (wire)} = 52.9\text{ MPa}\sqrt{m}$$

$$K_{Ic}\text{ (foil)} = 64.1\text{ MPa}\sqrt{m}$$

As before, the theory considerably overestimates the increase in the critical stress intensities, which were measured at 9.1 MPa$\sqrt{m}$ and 18 MPa$\sqrt{m}$ for the wire and foil reinforcements, respectively. More importantly, the theory predicts only a 21% larger critical stress intensity factor for the foil reinforced composite, where there was in fact a 100% larger value. This suggests that the morphology of the reinforcement should enter into the theory more comprehensively than simply as a volume fraction and thickness. Qualitatively, a significant difference exists between lamellar and linear reinforcements. When a crack propagating in the direction normal to a lamellar reinforcement impinges upon the reinforcement, the crack is arrested (at least briefly) while the reinforcement stretches and subcritical cracks nucleate on the opposite side of the reinforcement. Ultimately these subcritical cracks open wide enough that crack propagation continues until the next reinforcement is reached (this scenario produces the crack morphology seen in the 4-point bend specimen in Fig. 36). In a wire reinforced composite, a crack traveling normal to the wire direction is not arrested when it impinges on a wire. The crack simply travels around the wire and reconnects on the leeward side. At this point, the crack growth is slowed by the bridging effect of the wire, but there is no crack arrest-crack renucleation process as in lamellar composites. It should be noted that the K_{1c} specimens used in this study typically contained only 4-5 lamellae and 25-30 250 μm wires in the crack plane. The differences between the lamellar and linear reinforced composites will be even more pronounced in full-scale specimens which contain a larger number of reinforcements.

It is not obvious how to treat the morphological differences between lamellar and linear reinforcements theoretically. In light of the poor agreement of Eq. (22) with the measured K_{1c} values for wire reinforcements, the specific morphology for which the equation was developed, no attempt was made to modify the equation for lamellar reinforcements.

Figure 36. Typical crack morphology in a four-point bend specimen reinforced with 200 µm Nb foil, tested at 1100°C.

3.5 HIP Reaction Synthesis of Composites

One failing of the HIP and hot press methods for producing $MoSi_2$ composites is the relative lack of microstructural manipulation possible using these techniques. Pressure consolidation of $MoSi_2$ powder results in a predominantly single phase, equiaxed microstructure with an average grain size on the order of 50% of the original powder size. As a result, the only microstructural parameter that can be manipulated is the grain diameter, through control of the initial powder size. It is desirable to be capable of controlling a range of microstructural parameters, in order to explore the possibility of manipulating these parameters to control the mechanical behavior of $MoSi_2$. One means to achieve this control is through the introduction of a second phase into the microstructure, which will allow manipulation of grain morphology and size, $MoSi_2$/second phase volume ratio, and second phase chemistry. A simple, inexpensive approach is blending $MoSi_2$ powder with a suitable ternary elemental powder and reacting the powders during HIPing. Ti was chosen as the ternary element for the reaction HIPing because it is highly reactive with $MoSi_2$, reacts to form very high melting point silicides, and can produce a reduction in density.

3.5.1 $MoSi_2$ + Ti Based Composites

All metal powders used in this work were purchased from Cerac, Inc. The $MoSi_2$ powder was 99.5% pure, -325 mesh (i.e., 44 μm maximum diam). The Ti powder was 99.5% purity vacuum deposition grade, -150 + 325 mesh (44 μm < particle diam < 100 μm). The powder mixture was 90% $MoSi_2$ + 10% Ti by volume. All powder handling was done in high purity dry Ar, and powders were mechanically blended for 16 h prior to HIPing. Blended powder was packed into Nb tubes under Ar, vacuum degassed for 16 h, and electron-beam sealed. The packed tubes were then HIPed at 1400°C for 4.25 and 8.25 h under 207 MPa (30 ksi) pressure. Cubes approximately 10 mm on a side were cut from the consolidated material and compressed at 1300°C and 1400°C to ~ 24% total plastic strain in a vacuum of 10^{-5} Torr. A strain rate of $2 \cdot 10^{-4} s^{-1}$ was used, and the compression tests were interrupted before fracture occurred. Additional material was also produced for bend testing and fracture toughness testing by HIP reacting $MoSi_2$ + 7 vol% Ti and $MoSi_2$ + 20 vol% Ti at 1400°C/4 h/207 MPa. These specimens were bend tested in 4-point bending at room temperature, 1100°C, and 1250°C. Fracture toughness was measured at room temperature (see Fig. 27 for specimen geometries). The microstructure of the specimens was examined by SEM and TEM. EDX was used in both SEM and TEM to obtain localized chemical information from the specimens. TEM electron diffraction was used to determine the crystal structure of phases present in the specimens. Specimens were prepared for TEM from both as-HIPed and compression tested specimens by dimple grinding, followed by ion milling to electron transparency.

3.5.2 Microstructure

The quality of the $MoSi_2$ + Ti HIP reaction product was good, with 2-3% porosity. The general microstructure is shown in the optical micrograph in Fig. 37, for a specimen HIPed at 1400°C/207 MPa/8.25 h. The material is clearly two-phase, and the typical distribution of the phases can be seen in the SEM micrograph in Fig. 38. The $MoSi_2$ phase tends to be outlined in white, and appears raised in Fig. 38. Roughly 30% of the material transformed to a Mo-Ti-Si second phase in the $MoSi_2$ + 10 vol% Ti specimens. No differences were seen in specimens HIPed for 4.25 h compared to those HIPed for 8.25 h, indicating that equilibrium is reached within 4.25 h at 1400°C. The micrographs shown here are all from specimens HIPed for 8.25 h.

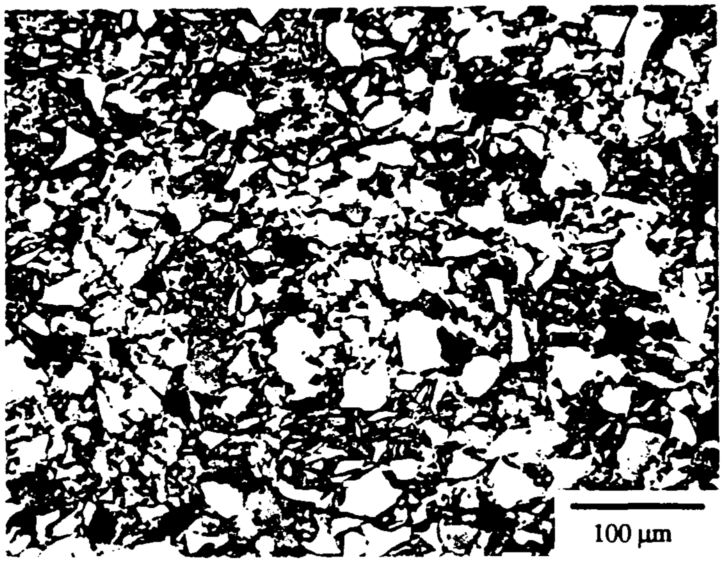

Figure 37. Optical micrograph of HIP-reacted $MoSi_2$ + 10 vol% Ti.

Figure 38. Typical distribution of phases in HIP reacted $MoSi_2$ + 10 vol% Ti.

A pronounced grain refinement effect was observed in the HIP reacted specimens. Figure 39 is a secondary electron image acquired in the TEM scanning mode. The difference in atomic number between Ti and Mo results in easily discernible contrast differences between the $MoSi_2$ and the Mo-Ti-Si phase, $MoSi_2$ being the lighter phase.

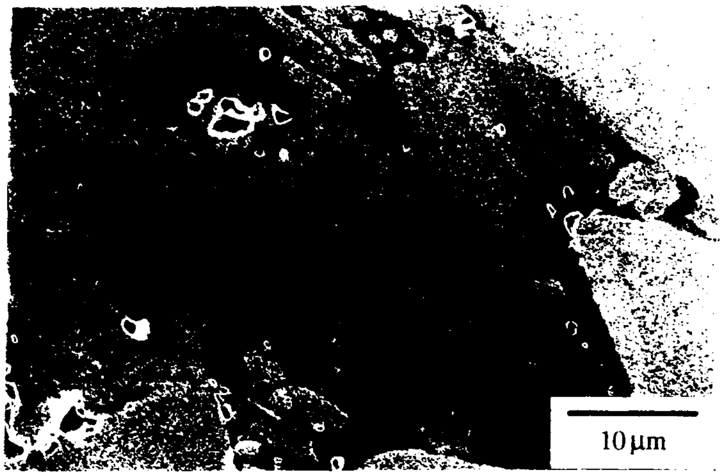

Figure 39. Secondary electron image of HIP reacted $MoSi_2$ + 10 vol% Ti. ($MoSi_2$ is the lighter colored phase.)

It can be seen that many of the $MoSi_2$ grains in contact with the Mo-Ti-Si phase are on the order of 1 μm diam, 10 times smaller than the average grain size seen in single phase $MoSi_2$ materials made from the same powder. Closer examination by TEM revealed that the second phase had an even greater degree of grain refinement. The TEM micrograph in Fig. 40 shows the structure of a typical second phase region. The second phase regions were typically composed of clusters of equiaxed, ~ 0.5 μm diam grains.

Figure 40. TEM micrograph of a typical second phase region in HIP reacted $MoSi_2$ + 10 vol% Ti.

3.5.3 Chemistry and Phase Identification

EDX spectroscopy was used to determine the distribution of Mo, Ti, and Si in the reacted specimens. No pockets of unreacted Ti were detected because the HIP reaction was done at 86% of the melting point of Ti, where Ti diffusivity is quite high. No Ti was detected in $MoSi_2$ grains, and the second phase chemistry was consistently measured to be 25 at.% Mo, 36 at.% Ti, and 38 at.% Si, within an error of 3 at.%. Electron diffraction unambiguously demonstrated that the second phase had the hexagonal $D8_8$ crystal structure, associated with a large number of 5-3 metal silicides. The measured lattice parameters of $a_o = 0.744$ nm and $c_o = 0.507$ nm are well within error of the parameters reported in Ref. 38 for $(Mo,Ti)_5Si_3$. Although a second hexagonal C40 ternary Mo-Ti-Si silicide exists (Ref. 48), this phase was never observed in our specimens. In terms of the 5-3 stoichiometry, the second phase is $(Mo_{0.42},Ti_{0.58})_5Si_3$ with an ideal density of ~ 5.9 g/cm^3, based on the measured lattice parameters. Using this density and the measured Ti concentration in the second phase, it can be calculated that 24% of the material should have transformed to $(Mo_{0.42},Ti_{0.58})_5Si_3$, in good agreement with the observations. Unfortunately, $(Mo_{0.42},Ti_{0.58})_5Si_3$ is only 7% less dense than $MoSi_2$, so the calculated density of the two-phase mixture is 6.2 g/cm^3, a very modest density reduction from 6.3 g/cm^3 for pure $MoSi_2$. The HIP reacted $MoSi_2$ + 7 vol% Ti and $MoSi_2$ + 20 vol% Ti specimens were weighed and measured to determine their density, which were 6.10 g/cm^3 and 5.95 g/cm^3 respectively. If the density of the HIP compaction is taken to be ~ 97% of the ideal value due to porosity, these measured densities correspond to porosity free densities of 6.29 g/cm^3 and 6.12 g/cm^3. These measurements confirm the minimal effect that alloying $MoSi_2$ with Ti has upon density.

3.5.4 Mechanical Behavior

The compression testing specimens showed no signs of cracking after compression to 24% strain at 1300°C and 1400°C. The yield stresses at the two temperatures were 186 MPa and 120 MPa respectively, showing no loss of strength compared to single phase $MoSi_2$. TEM examination of compressed specimens revealed that deformation took place only in the $MoSi_2$ grains (Fig. 41). The $(Mo_{0.42},Ti_{0.58})_5Si_3$ phase was always observed to be dislocation free, even when completely surrounded by highly deformed $MoSi_2$ grains. The lack of plastic deformation observed in the $(Mo_{0.42},Ti_{0.58})_5Si_3$ grains may indicate that these second phase regions accommodate strain through grain boundary sliding, a deformation mode

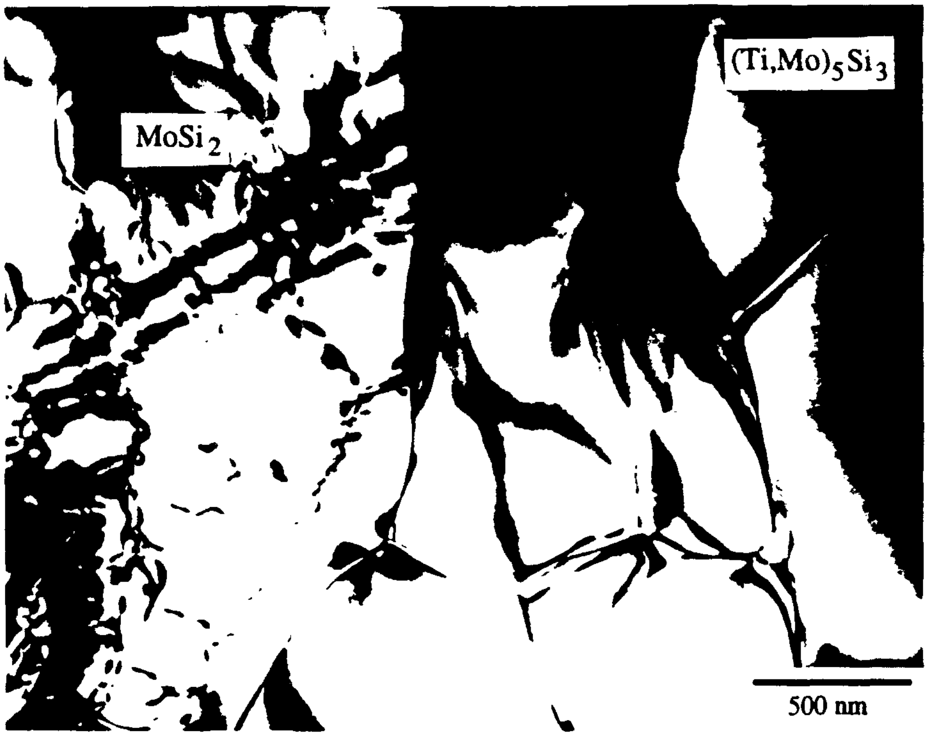

Figure 41. TEM micrograph of HIP reacted $MoSi_2$ + Ti compressed at 1300°C.

that may be assisted by the relatively slow strain rates and high temperatures used for the compression testing. Low-angle subgrain boundaries were observed in many $MoSi_2$ grains (Fig. 42), at a higher density than normally observed in deformed single phase $MoSi_2$. It is likely that the hard $(Mo_{0.42},Ti_{0.58})_5Si_3$ grains in contact with $MoSi_2$ grains act as nucleation sites for many of these subgrain boundaries, so the fine grain size of the second phase particles serves to refine the larger $MoSi_2$ grains by dividing them into numerous subgrains.

Figure 42. TEM micrograph showing high density of subgrain boundaries in an $MoSi_2$ grain in compressed $MoSi_2$ + Ti.

The results of the 4-point bend tests are shown graphically in Fig. 43, for both the $MoSi_2$ + 7 vol% Ti and $MoSi_2$ + 20 vol% Ti material. The material containing the higher amount of Ti had reduced strength compared to monolithic $MoSi_2$ (see Fig. 28), whereas the $MoSi_2$ + 7 vol% Ti had bend strengths comparable to monolithic $MoSi_2$. It was expected that the grain refinements and subgrain formation discussed in the previous paragraph would lead to strengthening by a Hall-Petch mechanism, particularly at elevated temperatures where dislocation mobility is greater. However, this strengthening effect was not observed, probably because it is offset by the inherent weakness of the $(Ti,Mo)_5Si_3$ phase which undergoes no plastic deformation even at 1400°C.

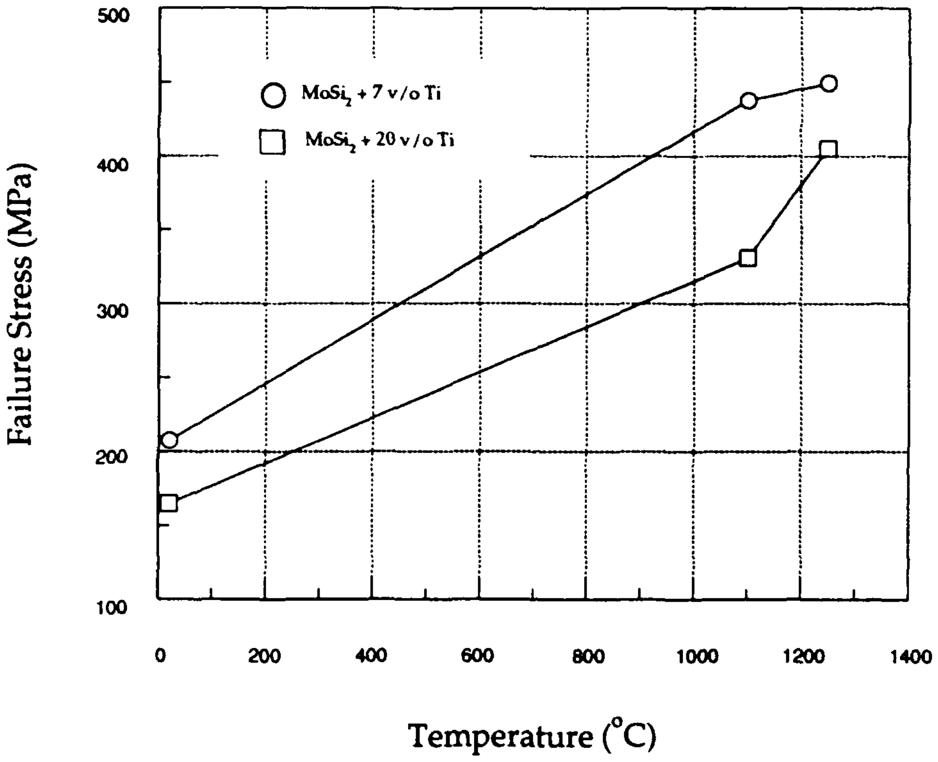

Figure 43. The four-point bend strength of $MoSi_2$ + 7 vol% Ti and $MoSi_2$ + 20 vol% Ti as a function of temperature.

The measured K_{Ic} values are tabulated in Table 8. A small difference was measured between the 7 vol% Ti and 20 vol% Ti specimens. The K_{Ic} values measured were ~ 20% below the values for monolithic $MoSi_2$ (see Fig. 29), so no toughening is produced by modifying the microstructure of $MoSi_2$ to include fine grained regions of the $(Ti,Mo)_5Si_3$ phase.

Table 8. Measured K_{Ic} Values for HIP Reacted $MoSi_2$ + 7 Vol% Ti and $MoSi_2$ + 20 Vol% Ti

Specimen	K_{Ic} $(MPa\sqrt{m})$
$MoSi_2$ + 7 vol%	3.2 ± 0.11
$MoSi_2$ + 20 Vol%	2.98

4.0 CONCLUSIONS

The major conclusions from the preceding study are summarized below.

1. Good quality, > 97% dense $MoSi_2$ and $MoSi_2$ composites can be produced by HIPing powder and powder reinforcement mixtures at temperatures as low as 1300°C.

2. HIP modeling is in good agreement with conclusion 1. Sensitivity analysis for the HIP modeling calculations show that the calculations are not sensitive to the grain boundary diffusion factor, δD_o, which is not a well established number.

3. Reaction between $MoSi_2$ and Nb reinforcements produces a complex two phase reaction zone. $MoSi_2$ and Nb react at a relatively slow rate at the projected use temperature of $MoSi_2$. For example, at 1300°C, it will take 144 days for a 200 μm diam Nb reinforcement to react until no Nb remains.

4. A significant loss in bend strength was observed in Nb-reinforced specimens, particularly at elevated temperatures. This was expected, due to the low elevated temperature strength of Nb. In general, improved toughness through ductile phase reinforcement will be accrued at the expense of elevated temperature strength.

5. Significant room temperature toughness increases were obtained by compositing $MoSi_2$ with Nb reinforcements. The reinforcement morphology had a large effect, and the morphologies are listed here in order of increasing potency: 200 μm spherical powder, 250 μm diam wire, 750 μm diam wire, and 200 μm foil.

6. Qualitatively, the observed toughening agreed with ductile phase toughening theory. However, when actual numbers are used, the quantitative predictions are highly inaccurate. This error is due to the current lack of detailed understanding of the crack energy absorbing phenomenon as it applies in particular to the $MoSi_2$/Nb system, and also to the failure of the theory to adequately account for reinforcement morphology.

7. HIP reaction appears to be a viable way to manipulate the microstructure of $MoSi_2$ composites, and is particularly effective as a grain refiner. However, HIP reacted $MoSi_2$ + Ti does not exhibit any improvements in mechanical behavior or density.

5.0 REFERENCES

1. M. F. Ashby: Acta Metall., 1975, Vol. 22, p. 275.
2. E. Artz, M. F. Ashby, and K. E. Easterling: Metall. Trans., 1983, Vol. 14A, pp. 211-221.
3. A. S. Helle, H. E. Easterling, and M. F. Ashby: Acta Metall., 1985, Vol. 33, p. 2163.
4. R. J. Schaefer: Int. J. Powder Metall., 1992, Vol. 28[2].
5. F. Garafalo and H. A. Wriedt: Acta Metall., Vol. 10, 1962, p. 1007.
6. A. K. Bhattacharya and J. J. Petrovic: J. Amer. Ceram. Soc., Vol. 74[10], 1987, pp. 2700-2703.
7. H. E. Deve, C. H. Weber, and M. Maloney: Mater. Sci. Eng., 1992, Vol. A155, pp. 19-31.
8. K. Sadananda, C. R. Feng, H. Jones, and J. J. Petrovic: Mater. Sci. Eng., 1992, Vol. A155, pp. 227-239.
9. S. M. Wiederhorn, R. J. Getteings, D. E. Roberts, C. Ostertag, and J. J. Petrovic: Mater. Sci. Eng., 1992, Vol. A155, pp. 209-215.
10. K. Sadananda, H. Jones, J. Feng, J. J. Petrovic, and A. K. Vasudevan: Ceram. Eng. Sci. Proc., 1991, Vol. 12[9-10], pp. 1671-1678/.
11. L. Xiao and R. Abbaschian: Mater. Sci. Eng., 1992, Vol. A155, pp. 135-145.
12. A. K. Vasudevan and J. J. Petrovic: Mater. Sci. Eng., Vol. A155, 1992, pp. 1-17.
13. S. Bose: Mater. Sci. Eng., vol. A155, 1992, pp. 217-225.
14. S. Bose and R. J. Hecht: J. Matls. Sci., 1992, Vol. 27, pp. 2749-2752.
15. W. O. Soboyejo, K. T. Venkateswara Rao, S. M. L. Sastry, and R. O. Ritchie: Metall. Trans. A, 1993, Vol. 24A, pp. 585-600.
16. B. W. Choi, Y. G. Deng, C. McCullough, B. Paden, and R Meharabian: Acta Metall. Mater., 1990, Vol. 38(11), pp. 2225-2243.
17. W. Kim, J. E. Flinn, J. G. Byrne: Acta Metall. Mater., 1993, Vol. 28, pp. 49-57.

18. J. Y. Kim, S. Okamoto, N. Uchida, K. Uematsu, K. Itakura, N. Uchida, K. Saito, A. Miyamoto, and T. Miyashita: J. Amer. Ceram. Soc., 1990, Vol. 73[1], pp. 74-78.
19. O. Unal, J. J. Petrovic, D. H. Carter, and T. E. Mitchell: J. Amer. Ceram. Soc., 1990, Vol. 73[6], pp. 1752-1757.
20. Plenum Press Handbook on High-Temperature Materials: New York, Plenum Press, 1964.
21. J. Schlichting: High Temp.-High Press., Vol. 10, p. 241 (in German).
22. O. Thomas, T. G. Finstad, and F. M. d'Heurle: J. Appl. Phys., Vol. 67[5], pp. 2410-2414.
23. H. J. Frost and M. F. Ashby: Deformation Mechanism Maps, Pergamon, Oxford, 1982.
24. E. K. H. Li and P. D. Funkenbusch: Mater. Sci. Eng., 1992, Vol. A157, pp. 217-224.
25. J. J. Petrovic and R. E. Honell: Ceram. Eng. Sci Proc., 1991, Vol. 12[9-10], pp. 1679-1689.
26. J. Besson and A. G. Evans: Acta Metall. Mater., 1992, Vol. 40[9], pp. 2247-2255.
27. M. F. Ashby: HIP487, Version HIP6.0, Cambridge University, U.K. (1990).
28. K. Uematsu, K. Itakura, N. Uchida, and K. Saito: J. Amer. Ceram. Soc., Vol. 73, 1990, pp. 74-78.
29. J. Y. Kim, S. Okamoto, N. Uchida, and K. Uematsu: J. Mater. Sci., Vol. 25, 1990, pp. 4634-4638.
30. Y. Oishi, K. Ando, and Y. Sakka: in Advances in Ceramics, Vol. 7, M. F. Yan and A. H. Heuer, eds., Amer. Cer. Soc., Columbus, Ohio, 1981, p. 208.
31. P. L. Martin, M. G. Mendiratta, and H. A. Lippsit: Metall. Trans., 14A, 1983, pp. 2170-2174.
32. S. L. Kampe, J. D. Bryant, and L. Christodoulou: Metall. Trans., 22A, 1991, pp. 447-454.

33. R. W. Hayes and B. London, Acta Metall. Mater.: 40[9], 1992, pp. 2167-2175.

34. K. Maruyama, T. Takahashi, and H. Oikawa: Mater. Sci. Eng., A153, 1992, pp. 433-437.

35. H. Oikawa: Mater. Sci. Eng., A153, 1992, pp. 427-432.

36. D. A. Wheeler, B. London, and D. E. Larson: Scripta Metall. Mater., 26, 1992, pp. 939-944.

37. H. N. G. Wadley, R. J. Schaefer, A. H. Kahn, M. F. Ashby, R. B. Clough, Y. Geffen, and J. J. Wlassich: Acta Metall., 39[5], 1991, pp. 979-986.

38. P. Villars and L. D. Calvert: **Pearson's Handbook of Crystallographic Data for Intermetallic Phases,** American Society for Metals, Metals Park, Ohio, 1985, p. 2772.

39. E. Fitzer and K. Matthias: High Temp. Sci., Vol. 3, 1971, pp. 93-98.

40. T. C. Lu, A. G. Evans, R. J. Hecht, and R. Mehrabian: Acta Metall. Mater., Vol. 39, 1991, pp. 1853-1862.

41. G. A. Cooper and A. Kelley: J. Mech. Phys. Solids, Vol. 15, 1967, p. 279.

42. G. A. Cooper: J. Mech. Phys. Solids, Vol. 18, 1970, p. 179.

43. W. W. Gerberich: J. Mech. Phys. Solids, Vol. 19, 1971, p. 71.

44. M. F. Ashby, F. J. Blunt, and M. Bannister: Acta Metall., Vol. 37, 1989, p. 1847.

45. K. T. Venkateswara Rao, G. R. Odette, and R. O. Ritchie: Acta Metall., Vol. 40, 1992, p. 353.

46. V. D. Krstic: Phil. Mag. A, Vol. 48, 1983, p. 695.

47. K. Suresh: Metall. Trans. A, vol. 16A, 1985, p. 249.

48. V. N. Svechnikov, Yu. A. Kocherzhinsky, and L. M. Yupko: Dokl. Akad. Nauk, Ukrain SSR, Vol. 6A, 1972, p. 566.

6.0 RESEARCHERS AND INSTITUTIONS INVOLVED IN PROGRAM

McDonnell Douglas Aerospace

D. S. Schwartz
R. J. Lederich
D. A. Deuser
J. D. Keyes

Washington University

S. M. L. Sastry
R. Suryanarayanan

7.0 PUBLICATIONS RESULTING FROM THIS PROGRAM

The following publications represent work performed under this contract.

1. D. S. Schwartz and P. J. Meschter, "High Temperature Deformation of $MoSi_2$," presented at TMS Annual Meeting, Anaheim, CA, February 1990.
2. D. S. Schwartz and S. M. L. Sastry, "Elevated Temperature Deformation Mechanisms in $MoSi_2$ and $MoSi_2$ + 20 vol% Nb," presented at TMS Fall Meeting, Cincinnati, OH, October 1991.
3. D. S. Schwartz, R. J. Lederich, D. A. Deuser, "HIP Synthesis of Two-Phase Mo-To-Si Alloys," Mat. Res. Soc. Symp. Proc. 288 (1993), p. 1075.
4. R. Suryanarayanan, S. M. L. Sastry, K. L. Jerina, "On the Values of Material Property Data Used in Hot Isostatic Pressing Models," Scripta Metall. Mater. 28 (1993) p. 797.
5. K. T. Venkataswara Rao, W. O. Soboyejo, and R. O. Ritchie, "Ductile Phase Toughening and Fatigue Crack Growth in Nb-Reinforced Molybdenum Disilicide Intermetallic Composites," Metall. Trans A 23A (1993), p. 2249.
6. W. O. Soboyejo, K. T. Venkataswara Rao, S. M. L. Sastry, and R. O. Ritchie, "An Investigation of Ductile Phase Reinforcement on the Fatigue and Fracture Behavior of Advanced High-Temperature Intermetallics," Metall. Trans. A 24A (1993), p. 585.